Failure Properties and Phenomena for Zircaloy-4 from Ring Compression Testing

A Thesis Presented for the
Master of Science
Degree
The University of Tennessee, Knoxville

Benton Edward Garrison
December 2018

ACKNOWLEDGEMENTS

I would like to express my sincere gratitude to my advisor, Dr. Stephanie TerMaath for her guidance through the research and writing of my thesis. With her extensive knowledge to overcome the technical obstacles and her patience and enthusiasm for motivational support, I could not have asked for a better advisor or mentor.

Thank you to Dr. Yong Yan for his mentorship and continuous support at ORNL during my MS study, and for sharing his technical knowledge as they pertained to my studies. Also, thank you for access to materials and equipment that made the work in this thesis possible.

Thank you to Mahmut Cinbiz (Nedim) for technical information and helpful discussions.

Thank you to my family and close friends that supported me through this education and my life in general.

Thank you to Judy King from OIT for her help making the MS thesis template.

ABSTRACT

An effective method to determine the plastic strain at fracture and investigate the fracture energy of as-received and hydrided unirradiated Zircaloy-4 tubes in the hoop direction at room temperature was developed for ring compression tests through experimental and computational evaluation. The hydrogen content was varied up to 610 weight parts per million so that failure was consistently ductile. A Gurson-based approach for ductile damage was used to model material failure. Experimental test results and computational simulations modeled in Abaqus were integrated to directly determine plastic strain at fracture, and empirical fitting was used to investigate fracture energy. As expected, increasing hydrogen content caused embrittlement of the Zircaloy-4 samples tested and the plastic strain at fracture and fracture energy to decrease. The developed procedure was demonstrated to directly determine plastic strain at failure and indirectly evaluate comparative fracture energies.

TABLE OF CONTENTS

LIST OF TABLES

LIST OF FIGURES

1. INTRODUCTION AND GENERAL INFORMATION

1.1 Introduction

Nuclear cladding encases the fuel and acts as the first barrier against the release of nuclear material, especially during operation and transportation/storage of spent nuclear fuel (SNF). As such, retention of the cladding's mechanical integrity is crucial to prevent nuclear material release. This becomes more challenging after reactor operation, where the high-temperature environment promotes hydrogen ingress, which eventually compromises the tube-shaped cladding's ductility.

The phenomena describing hydrogen embrittlement of nuclear fuel cladding has been well-established in the literature for years. In summary, hydrogen absorbed by the metal matrix precipitates to form brittle hydride platelets when the metal cools, reducing the ductility of the material [1-9]. The degree of this mechanical degradation from hydrides depends mainly on two factors: hydrogen concentration and hydride orientation [1-9]. Hydrogen concentration has been known to diminish the ductility around room temperature through increasing the hydride density [1,2,4,7-9], while reoriented hydrides introduce a low-energy fracture path by exposing the weaker hydride-metal interface to the larger circumferential stresses [4,5,8,9]. Since the discovery of the severity of radial hydrides, material and tube fabrication processes have been optimized to inhibit hydrogen ingress (reducing hydride density), and material states that motivate radial hydride orientations are more readily avoided (reducing possibility of radial hydrides) [10-13]. With these new cladding alloys in mind, determining properties of relatively low concentration, circumferentially hydrided materials have become a more relevant part of the discussion.

After reactor operation, the cladding assemblies are eventually loaded into concrete casks and transported offsite [4,8,9,13], subjecting the cladding to various loads. Typically, testing the safety of the SNF involves mechanical property studies including axial tension, ring-stretch, ring compression, and biaxial tube burst tests, which represent in-situ conditions of the cladding and fuel pellet structure during transportation and storage [7,14,15]. Even though the fuel pellets inside the cladding tube influence the mechanical response of SNF, the cladding is commonly tested on its own because the composite structure significantly increases the complexity of mechanical tests, and the ductility of the cladding on its own still plays a crucial role in SNF safety [14,15].

In the nuclear industry the ring compression test (RCT) has been used by the Nuclear Regulatory Commission (NRC) to determine cladding tube ductility in the circumferential direction [16], an important property in evaluating the likelihood of cladding failure and possible fissile material release. In general, this test method was developed to minimize the work required on the sample—an important feature when handling irradiated material—and the similarity of the test to in-situ loading events during transportation and storage after cladding is retired from reactor use. Despite its convenience and applicability, ring compression testing does have some shortcomings. Specifically, displacement rates are generally held constant during RCTs, but because of large geometry changes, this loading condition corresponds to an inconstant strain rate making strain-rate sensitivity hard to quantify. Further, obtaining material properties from the test typically requires an assumption that properties are isotropic and the same in compression and tension [7]. Finally, the maximum load is isolated to a small region that makes experimental strain values at this location difficult to measure [7]. Therefore, most methods to determine strain values from RCTs rely on finite element modeling [7].

Attempts have been made to obtain anisotropic properties from RCTs, but there are difficulties in empirically fitting multiple parameters especially if they change with plastic deformation [17]. To this end, unless anisotropic tensors are known beforehand, finite element modeling with RCTs is used to determine yield stress and Young's modulus and then empirically fitting to experimental data is applied to accurately simulate the strain-hardening portion of the stress response to a Holloman relation, all under an isotropic assumption [4,6,18-24]. After fitting the Holloman parameters to RCT results, works in the literature cut-off simulated results at the same displacements where experimental specimens failed, but an established method to determine failure properties like plastic strain at failure and fracture energy was not developed.

Although using the exact tensor would be ideal when modeling the mechanical response of the material, determining that tensor poses many difficulties. One way to determine the anisotropic tensor would be to take the tensor from the as-received material and adjust it based on the environments it experiences. Tracking these anisotropic properties through the entire life of the cladding would require intensive book-keeping, and the final properties would be accompanied by errors from imperfect models or imprecise environment characterizations during reactor use. Another approach would be to directly measure these properties with post-reactor materials. This approach requires exhaustive setup and testing to produce stress states that could isolate the 6 independent components of the plasticity tensors developed in the literature [10,17]. Extensive testing requires more material and a great deal of funding, and it becomes even less attractive with multi-phase layers from oxidation, fuel pellet-cladding bonding, precipitates, and other features created throughout the cladding's life. Due to these difficulties, a method that can determine isotropic mechanical properties including plastic strain at cladding failure during RCT gains merits provided that the errors accompanying the employed assumptions are acceptable relative to the cost and errors of the other methods. To this end, a Gurson-based damage model was implemented in this work to obtain the equivalent plastic strain at fracture and estimate the fracture energy of Zircaloy-4 (Zry-4) nuclear cladding with varying concentrations of circumferential hydrides. The addition of this model will more precisely determine ductility parameters of SNF specimens, and with some improvements has the potential to combine damage from the various types of loadings present in SNF transportation and storage.

2 LITERATURE REVIEW

2.1 Nuclear Materials

2.1.1 Zirconium in the Nuclear Industry

Nuclear fuel cladding encases the nuclear fuel in the reactor; therefore, it is the first barrier against fuel release during operation, transportation, and storage. As such, maintaining the cladding structural integrity is crucial to ensuring the safety of these procedures [13,15]. Zirconium-based alloys have been used as cladding materials in nuclear reactors primarily because their high-temperature corrosion resistance promoted more favorable mechanical properties after reactor service, and their low thermal neutron cross-section maintains the correct neutron and thermal economies to promote chain reactions [10-12]. With the backing of the nuclear industry, these materials were developed into alloys with improved corrosion resistance and mechanical performance while still maintaining satisfactory neutron conditions mainly by alloying with different elements or altering the forming processes [10-12]. Since reactor operating conditions vary based on design, specific improvements are not always suitable to the entire set of cladding alloys. To this end, Zircaloy-2 and Zry-4 emerged as successful developments that are still used in modern reactors.

More recently, newer zirconium-based alloys have been developed to further optimize cladding performance to allow for higher burnups, namely Zirlo, Duplex, M5, and E110 [10-12,26]. To produce higher energy yields in the future, the Gen IV reactors currently in development will be operated at even higher burnups, and novel corrosion-resistant alloys have been invented (i.e. FeCrAl) [12]. With this outlook on the future of nuclear energy, the cladding candidates for Gen IV reactors do not use zirconium as the base metal with a few exceptions [12]. Despite their possible exclusion in the next ages of nuclear reactors, zirconium alloys and their mechanical response during transportation and storage will remain a necessary topic in the coming years for the safe deposition of the spent nuclear fuel from current reactors.

2.1.2 Zry-4 as cladding material

Zry-4 has been used as the cladding material in pressurized water reactors (PWR) and light water reactors since its development. As a zirconium-based alloy, Zry-4 exhibits hexagonal close-packed (hcp) crystalline structure, resulting in limited slip planes and higher anisotropy relative to metals with cubic structures [10,27]. Furthermore, the fuel is stacked in cylindrical shapes to avoid critical masses or geometries, thus a tube-shaped cladding is needed to contain the fuel. The tube-forming processes create strong texture in the cladding, meaning that grain orientations are not all the same [10,27]. The combination of hcp crystal structure, tube-forming texture, and annealing produces increased anisotropy from various sources, which requires a multi-component tensor to describe the mechanical properties exactly.

2.1.3 Hydrides

Under accident and operating conditions in water-cooled reactors, waterside corrosion generates an oxide layer on the cladding surface, and hydrogen is released as a byproduct of the oxidation reaction [1-9]. Operating temperatures then motivate hydrogen ingress into the metal. When the metal cools, the solubility limit of hydrogen decreases, thus hydrogen picked up in the metal matrix precipitates to form brittle hydride platelets reducing the ductility of the material [1-9], which is mostly attributed to the decreased stresses required for hydride-matrix separation [1,3,4]. The degree of this mechanical degradation from hydrides depends mainly on two factors: hydrogen concentration and hydride orientation [1-9].

Increasing hydrogen concentration has been known to diminish the ductility through increasing the hydride density. The significance of higher density is a statistical increase in hydride-hydride connectivity, so a smaller portion of circumferential loads are being carried by the ductile metal matrix [1,4]. To demonstrate this behavior, figure 1 taken from Yan [1] and Kim [4], below shows micrographs of varied hydride concentrations in

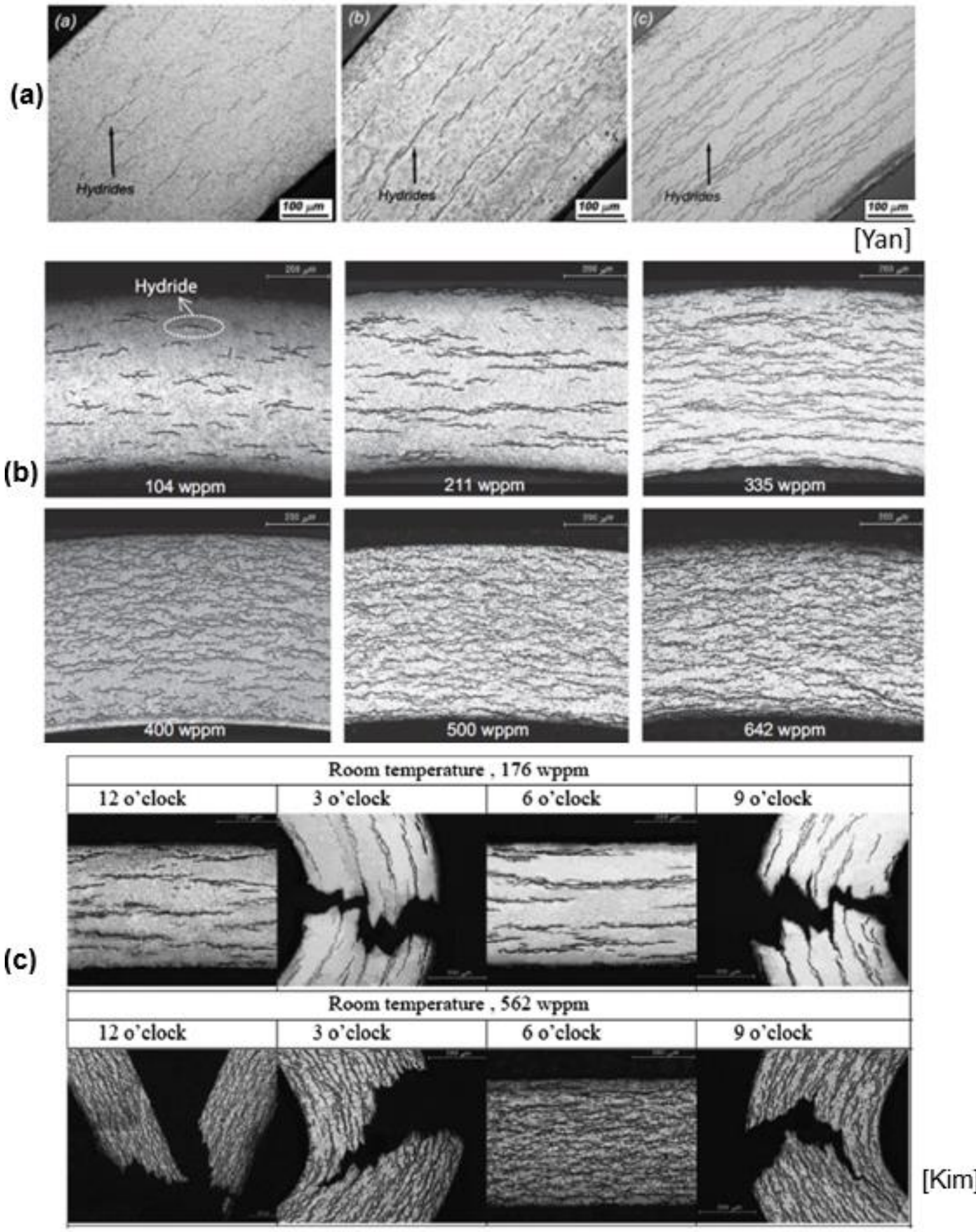

Figure 1. Micrographs from: (a) Yan [1] and (b) Kim [4] depicting hydrided Zry-4 material with circumferential hydrides of varying concentrations. (c) depicts the fracture path across the tube wall thickness. Of note is the quality of the crack to travel in the wall thickness direction unless a circumferential hydride is present where the crack can propagate along the hydride-metal interface in the circumferential direction [4].

Zry-4 material as well as the crack path across the tube wall thickness. Among other things, the discovery of hydride embrittlement in zirconium alloys has led to the development of alloys and optimization of fabrication processes that inhibit hydrogen ingress resulting in lower hydrogen pickup during reactor use.

If a circumferentially hydrided zirconium-alloy tube is exposed to moderate temperatures and certain stress states, the hydrides can be reoriented such that the hydride platelet normal is in the circumferential direction instead of the radial direction [1,4,5,8,9] as shown in figure 2 from Kim [4]. Radial hydrides present a lower-energy fracture path where circumferential stresses can separate the weaker hydride-matrix interface in the radial direction [1,4,9]. Similar to the progress made to reduce hydrogen concentrations, tube fabrication processes and post-reactor environments have also been optimized to avoid material states that motivate hydride reorientation. As a result, determining mechanical properties and failure conditions of lower hydrogen concentration samples with circumferential hydrides becomes a more relevant part of the discussion.

The holistic approach to investigate the mechanical performance of hydrided material is to combine the mechanical properties of the hydrides, hydride-matrix interface, and the anisotropic metal matrix with a hydride density characterization to obtain more realistic local mechanical responses. A recent Gurson-based model by Le Saux et al. [3] achieves this with exceptional success, and recent [28] and future models that improve characterization of anisotropy and plastic flow could further improve these approaches. These methods provide the groundwork for insights into the material

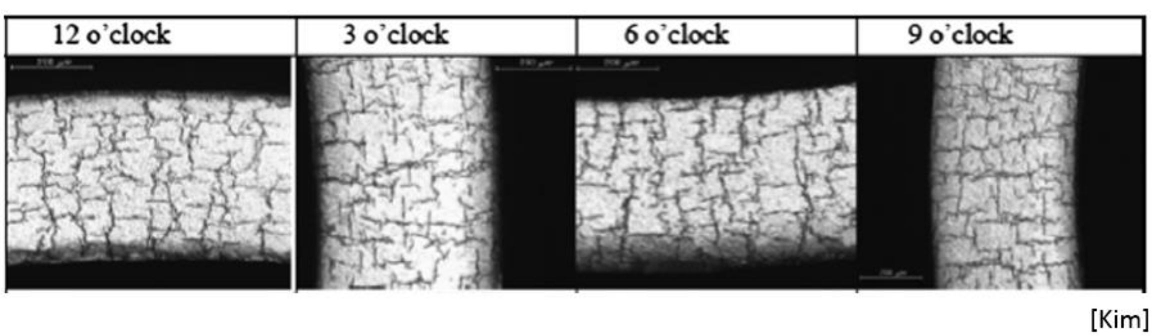

Figure 2. Micrographs from Kim [4] showing Zry-4 at 137wppm with reoriented hydrides. path across the wall-thickness of hydrided Zry-4. Of note is the fracture path along hydrides before continuing in the radial direction.

behavior that drive material improvements, but they become increasingly difficult and expensive for evaluating irradiated materials.

Various experimental procedures to calculate or measure the mechanical properties of cladding tubes are implemented because they can isolate material properties in single directions or mimic stress states or loading conditions of real and postulated failure modes. As stated before, those that isolate some of the anisotropic mechanical properties, while important, become less attractive with more expensive materials because extensive testing is required to completely characterize the material. For this purpose, those methods will not be discussed in detail here. Other mechanical testing methods are developed to test against specific accident conditions, including but not limited to Reactivity Initiated Accidents (RIA) [2,7], Loss of Coolant Accidents [29,30], and conditions that might cause loss of nuclear material during transportation and storage after reactor use. Desquines et al. [7] provides a thorough summary of these methods, although it is mostly to describe their applicability to RIA events. Among the methods described there is the RCT, which due to the lower cost and resemblance to actual cladding loads during storage and transportation, is also used in SNF campaigns.

2.1.4 SNF storage and transportation

After cladding is retired from reactor use, the fuel assemblies, large structures to hold multiple cladding tubes in an array then stocked in concrete casks that are loaded onto trucks and transported off-site. This process is shown in figure 3.

In the event that a tube breaks, the fissile material within could conglomerate and create a mass or volume that reaches criticality. During the transportation and storage process, the assemblies—and thus the cladding—are subject to various loads that may compromise their integrity. Currently, to evaluate the likelihood of mechanical breakage, these loads are recreated through axial tension, ring compression, ring extension, and tube burst tests [13,15].

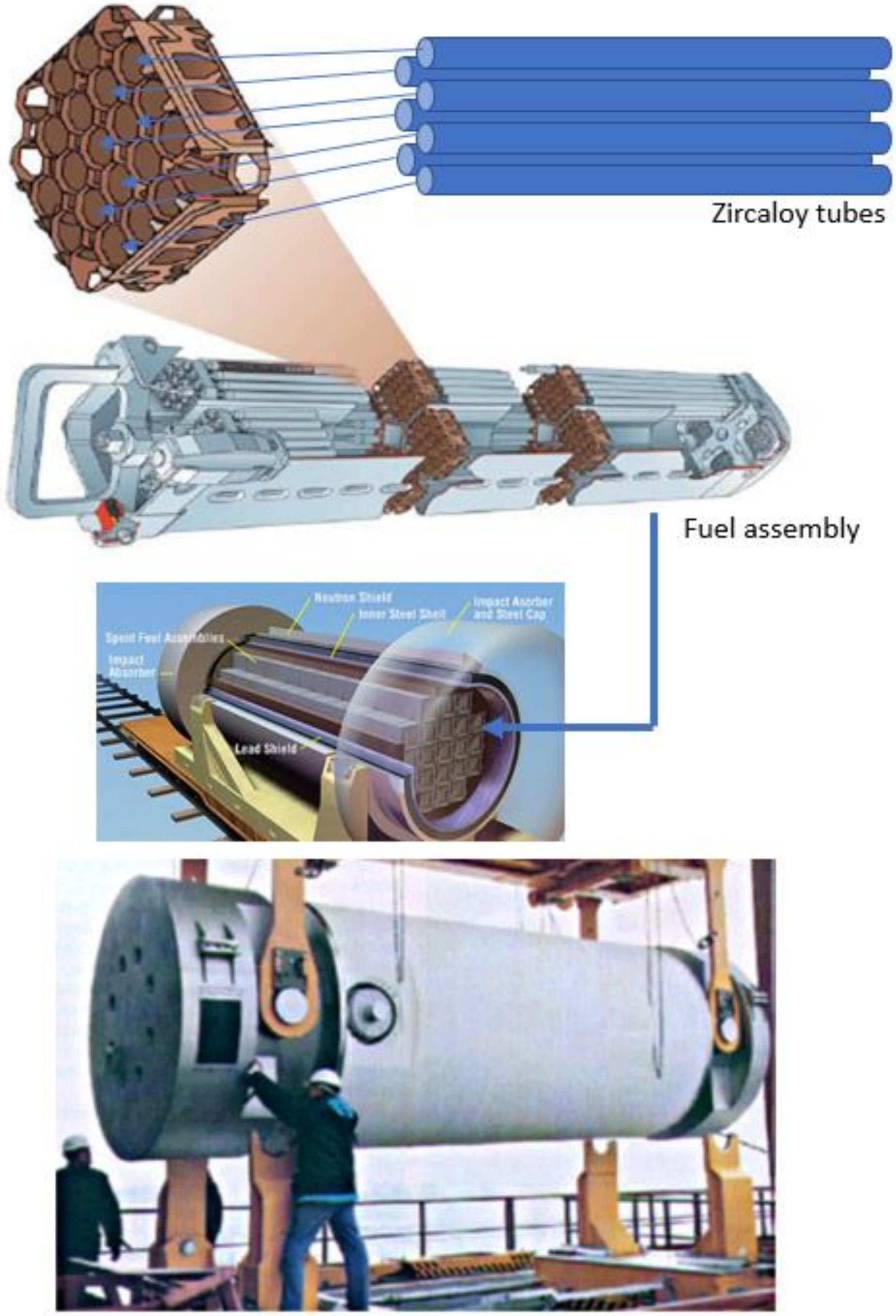

Figure 3. Fuel assembly structure and cask to store spent nuclear fuel. These casks are eventually loaded onto a truck and transported off-site to be stored above ground indefinitely. Assembly, Cask and loading images taken from [31], [32], and [31] respectively.

2.2 Ring Compression Tests

2.2.1 Origins

Most of the early literature on RCT is with aluminum or other metal alloys for their use as possible energy absorbers for vehicle impact [20,33,34]. The major works by Deruntz/Hodge [33], Burton/Craig [34], and Redwood [35] introduced analytical models for RCT based on different modes of collapse ultimately producing an equation to calculate Young's modulus from Deruntz/Hodge [33] that is still in use today. Reid and Reddy [18-20] built on those works to develop a comprehensive RCT investigation involving experimental work and intense applied mechanics to better reproduce experimental results, obtain some mechanical properties, and explain various unique structural geometries that are observed throughout the tests. Their model incorporated the traveling hinge on the top, flattening portion of the tube, a deformable circular arc around the 3 o'clock position, and a rigid circular arc that connects the other two components shown in figure 4 [18,19]. The combination of these three components makes up one quadrant of the ring.

Despite their model's reasonably accurate predictions, they stated that the use of a mean strain hardening modulus was the likely source of the errors present in their analysis. It is worth noting that discrepancies between their theory and experimental results were negligible for mild steel but were significantly larger for Zry-4, and errors

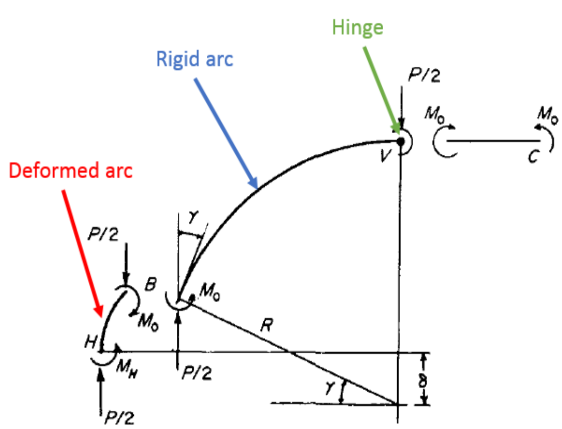

Figure 4. Analytical model from Reddy and Reid [18]
to calculate yield stress and estimate RCT response

were negligible at early displacement stages of the RCT but became more significant as the displacement was increased [19]. As expected from their errors in matching the load-displacement RCT data, their reported plastic strain calculations agreed well with those measured by strain gauges for low RCT displacements with mild steel but started to diverge as plastic strain increased. They did not report calculated or experimental strains for Zry-4 specimens, but due to larger discrepancies in the global behavior, calculations with Zry-4 are expected to be less accurate than those with steel.

2.2.2 Modeling

Following the analytical groundwork by Reddy and Reid, the next developments focused on finite element modeling (FEM). Leu [23] performed 2D finite element analysis to study the effect of various parameters on load-displacement results, buckling ratio, and ring shape of aluminum rings. However, they did not match their ring shape/buckling to experimental data because they used other researchers' experimental data, and they did not investigate any combined effects of these parameters. Nemat-Alla [21] and Rathnaweera [22] developed iterative algorithms to fit simulated load-deflection curves to experimental curves, which allowed them to determine strain-hardening properties of Brass and aluminum tubes from RCT. Bizet et al [24] used a Rayleigh distribution to assign probabilistic yield stress properties to each element to model macroscopic material behavior and show how modifying just one property improves modelling of macroscopic materials in RCT and axial tension testing of aluminum alloys. In their experiments they used Digital Image Correlation (DIC) to measure physical strains to compare with simulated strains and determined material properties from each test. They also found that there were significant errors when transposing material properties found from one test to a different test. However, it was only significant (>8%) when transposing properties from tension tests to ring compression tests.

Except for Reid and Reddy's work, the deficiency in all of these more recent works as they apply to nuclear claddings is that they were never tested to failure, so a method to determine the strain at fracture was not developed. While Reid and Reddy did investigate calculating plastic strains, their use of the average strain-hardening parameters was too imprecise for plastic strain calculations at later deformations. Furthermore, the critical strain location is isolated at the 3 o'clock and 9 o'clock OD positions, making experimental strain values unreliable with conventional strain gages [7,18].

2.2.3 RCT for Nuclear Materials

In the nuclear industry, the RCT, has been used by the NRC primarily as a screening test to determine cladding tube ductility in the circumferential direction [7,16,36].

For nuclear materials, Yamada et al [17] employed FEM to Zry-4 by using Hill's yield criterion to incorporate anisotropy. However, they did not match experimental results within a reasonable error, because the 6 components of the Hill's criterion need to be updated based on hydrogen concentration and plastic deformation. It is prohibitive to find properties of 6 interdependent variables. Despite the shortcomings, some of which was because of the lack of high-power computational facilities at the time, their work produced more qualitative features of RCTs, specifically those from anisotropy. Kim et al [4] investigated the hydrogen embrittlement during RCTs of Zry-4 tubes where they followed the procedure of calculating yield stress and elastic modulus from experimental tests and used a power law relation to model plastic behavior. Both of those works were with 2D simulations, and no methods to determine plastic strains or fracture properties were reported.

Rengel [6] has modelled the failure of unirradiated hydrided Zirlo specimens by using a small layer of cohesive elements in the failure location of the tubes with 2D simulations. In that work, they iterated through simulations to find the cohesive-equivalent, heterologous properties, so their simulations could reproduce the experimental load vs displacement curve. Despite their strength in reproducing RCT data, there is difficulty in translating material properties modeled by delamination to properties for void nucleation, growth, and coalescence. To illustrate, the properties from the literature and Rengel's work are shown in Table 1 below. This difficulty stems from cohesive elements' inability to model the substantial axial direction strains, and the inclusion of the cohesive-metal interface in the simulation that interrupts the continuum.

Furthermore, their method requires an iterative algorithm to find multiple fracture properties, resulting in the potential for future development of a direct method.

2.2.4 Ductile Damage model

To avoid interrupting the continuum and to better model the realistic complex stress state at the failure location, a material model that can be used in conjunction with the standard stress elements is required. Recent plasticity and fracture models were developed that includes fracture strain's dependence on stress state [37-40]. In those models, the stress state was described by the stress triaxiality (ST), which was defined as the ratio of hydrostatic stress to the Von Mises equivalent stress as shown in equation 1

$$ST = \frac{\sigma_1+\sigma_2+\sigma_3}{\sqrt{\left(\frac{1}{2}[(\sigma_1-\sigma_2)^2+(\sigma_2-\sigma_3)^2+(\sigma_3-\sigma_1)^2]\right)}} \qquad (1)$$

where σ_1, σ_2, and σ_3 denote the principal stresses [37]. For comprehensibility, a chart from [38] is attached as Table 2 that shows the various ST values at common stress states. With this stress state description, equivalent plastic strain, a scalar culmination of strain rate, history, and stress state, can be expressed empirically as a function ST.

The integral criterion, shown in equation 2 (notation consistent with Abaqus)

$$\omega_D = \int_0^{\varepsilon_{eq}^p} \frac{d\varepsilon_{eq}^p}{\varepsilon_{eq}^p(ST)} = 1 \qquad (2)$$

where ω_D is the damage initiation criterion used to determine if failure has initiated. Specifically, once the total damage reaches unity, the element will begin losing load-loss capability. In Abaqus, the damage value is updated incrementally following equation 3 from Abaqus documentation [41]

$$\Delta\omega_D = \frac{\Delta\varepsilon_{eq}^p}{\varepsilon_{eq}^p(ST)} \geq 0 \qquad (3)$$

so the damage at each analysis increment is summed until unity. Since damage is updated incrementally, damage sustained at one stage of a mechanical test can still be

included in the fracture initiation response at a later stage even if the stress state changes (except for severe load path changes like tension-compression reversal [37]). Therefore, the combination of the equivalent strain function and damage criterion acts as a phenomenological failure process that can aggregate how much damage an element has sustained from previous stress states that includes sensitivity to stress state.

This model has been successfully implemented in quasi-static and dynamic crash simulations of aluminium [37] and even in the nuclear industry for drop tests of steel canisters [38]. It is important to note that other works have improved the model from its base form with lode-angle dependence [39]. The damage model is tested in its base form in this work as a proof of principle, but there is potential for more precise analyses with damage model improvements in the future.

Table 1. Yield stresses obtained from literature, solid elements in FEM, and cohesive elements in FEM.

Source	Yield Stress (MPa)
Literature	600-800
RCT calculations	800
Cohesive method	900

Table 2. Examples of stress triaxiality factor, ST (denoted TF by source), calculations with their conventional name in the description from Snow [38] used to characterize the stress state.

Normalized Principal Stresses			ST	Conventional name
σ_1	σ_2	σ_3		
1	0	0	1	Uniaxial Tension
1	1	0	2	Biaxial Tension
1	1	¼	3	Triaxial Tension
1	½	½	4	Triaxial Tension
1	1	1	∞	Triaxial Tension
1	-1	0	0	Tension/Compression
1	-1/2	0	0.378	Tension/Compression
1	1	-1	0.5	Biaxial Tens./Comp.
1	-1	-1	-0.5	Tens./Comp./Comp.
-1	-1	-1	-∞	Triaxial Compression

3 MATERIALS AND METHODS

3.1 Materials

This study focused on PWR cladding tubes manufactured with Zry-4. Hydrogen contents ranged from as-received (~15 wppm) to 610 wppm. Material processing to prepare the tubes for PWR operation was expected, but the cold-work and annealing history of the material was not specified. The specific cold-work and annealing histories were not specified, but the tubes were described by the vendor as ready for a PWR. The tubes in this work had a wall thickness of 0.57 mm, an outside diameter (OD) of 9.51 mm, and the lengths were >10mm. Table 3 shows the material composition of the Zry-4 used in this work.

3.2 Methods

3.2.1 Hydriding Procedure

The hydriding system consists of a furnace with a sealed chamber that was brought to a vacuum, purged with argon, filled with hydrogen gas, then heated to 400-450C to promote hydrogen ingress into the cladding tubes. The system was optimized to produce the desired hydrogen contents based on the pressure of hydrogen in the chamber. The environment was left unaltered until the samples cooled to room temperature after the furnace was turned off. The hydrogen contents were measured using the Inert Gas Fusion technique abiding by ASTM E1447-05. More information on the hydriding system can be found here [1].

Table 3. The material composition of the Zry-4 cladding used in this work. Compositions are reported in mass fraction and were determined by combustion methods [1].

Alloy	Fe	Sn	Cr	Si	O	Hf	Al	Ti	Zr
Zry-4	0.22	1.26	0.1	0.01	0.13	-	-	-	Balance

3.2.2 Ring Compression Testing

An RCT [1,4,6,16,17-24] consists of compressing a tube laterally between two steel plates as shown in figure 5. Experimental RCTs were performed on an Instron 5966 at room temperature, and the crosshead speed was kept constant at 2mm/min.

3.2.3 Simulations

RCT simulations were performed using an Abaqus 6.14-2 Explicit procedure, because explicit analyses are better-suited at handling large deformations and contact. Explicit analyses for quasi-static testing typically accelerate loads to significantly reduce runtimes, so special care must be taken to ensure that dynamic stress effects are omitted from results. When defining loads in explicit models, Abaqus generally recommends keeping impact velocities lower than 1% of the material's wave speed [41]. The typical wave speed of metals, 5000 m/s (or 5E6 mm/s), [41] was considered. Under the assumption that Zry-4 would be within 1 order of the typical metal wave speed, impact velocities around 500 mm/s were deemed acceptable. In this work, platen displacements, therefore impact velocities, were defined at 600mm/s to match the elastic and pre-damage plastic portions of RCT simulations. In some cases, displacement speeds were reduced to 200 mm/s if the creation of cracks created qualitatively significant oscillatory load

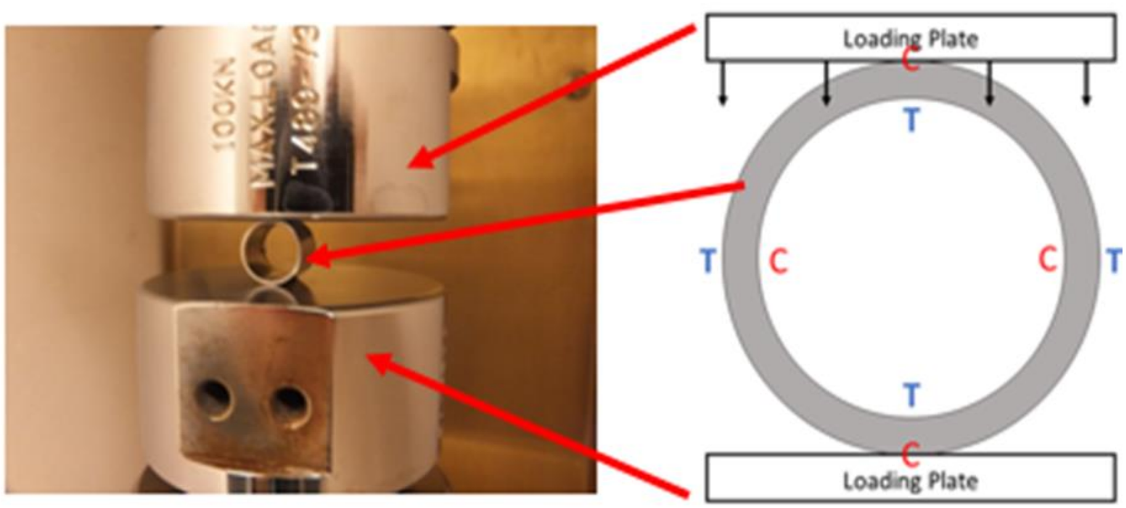

Figure 5. Image of an RCT with a diagram showing loading plate direction and general stress states at the most important 12, 3, 6, and 9 o'clock locations. C denotes compression, and T denotes tension.

responses. Furthermore, energy histories can be output from Abaqus simulations to ensure that the simulation is dominated by the quasi-static response instead of the dynamic response. Particularly, this is performed by checking that inertial and kinetic energies of the material being modeled are negligible compared to the internal energies (stored energy through material stresses). An energy output result from this work is shown in figure 6, which shows that the dynamic energies were indeed negligible compared to the internal energies.

Simulations in 2D and 3D were performed to investigate length dependence effects and qualitatively verify the material model. Specifically, 2D simulations were used because they have significantly reduced run-times. However, because 2D simulations ignore changes in the length dimension, 3D simulations were required for length-dependence studies. In this work, since samples were longer than their OD, a plane strain state was defined in 2D simulations [18-20]. Simulations in 3D were performed to verify that the determined material properties were length-independent, which was especially critical for fracture properties. Due to the RCT symmetries, only 1/8 of the sample was modeled for 3D simulations, and symmetric boundary conditions were applied. Symmetries were not employed in 2D simulations. Images from both simulation types are shown in figure 7.

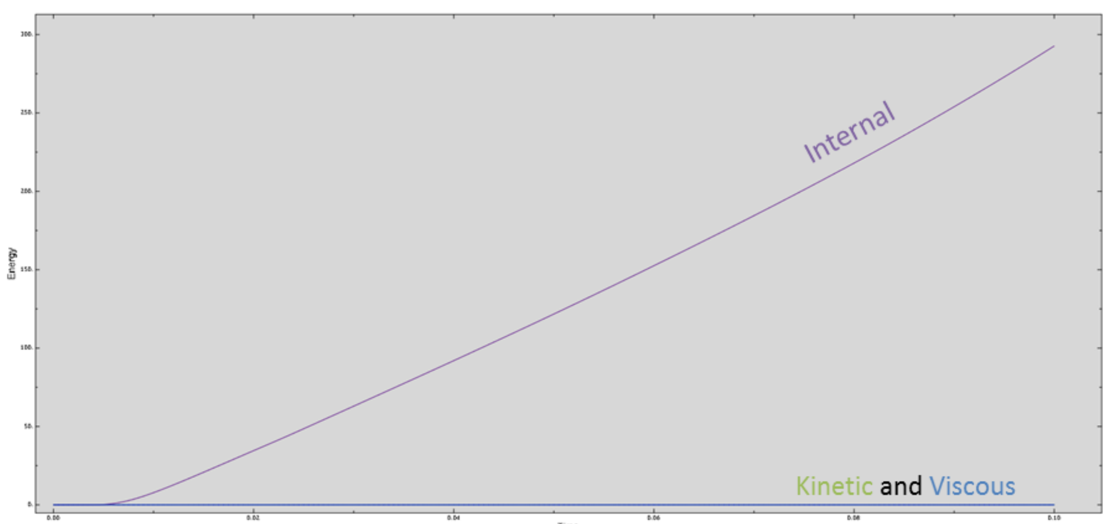

Figure 6. Energy outputs from simulations showing that dynamic energies are insignificant compared to internally energy, proving that simulations were quasi-static.

In 2D simulations, linear quad elements were used with second-order accuracy and element deletion features enabled, and they were meshed with a structured technique. The remaining values were left as their defaults. In 3D simulations, linear hex elements were used with second-order accuracy, element deletion, and reduced integration features enabled, and they were meshed with a structured technique. Preliminary 2D simulations showed unnatural wavy behavior throughout the ring cross-section at high displacements as shown in figure 8. This was remedied by the options in the precision tab of the job editor. Specifically, the Abaqus/Explicit precision was set to double and Nodal output precision was set to full. This addition was found to also reduce run-times, so it was implemented for 3D simulations as well.

Mesh convergence studies were performed for 2D and 3D simulations. For all simulations the mesh density was biased so the element length in the circumferential direction was equal to the length in the wall-thickness direction at the 12 o’clock, 3 o’clock, 6 o’clock, and 9 o’clock positions, and gradually increased to three times the wall-thickness direction length at the midpoint between those locations. For 3D simulations, the axial-direction length was the same as the wall-thickness direction length. Based on these schemes changing the number of elements in the wall thickness dimension also refines the mesh in the circumferential and axial dimensions. For 2D simulations it was observed that at least 8 elements through the wall-thickness (radial

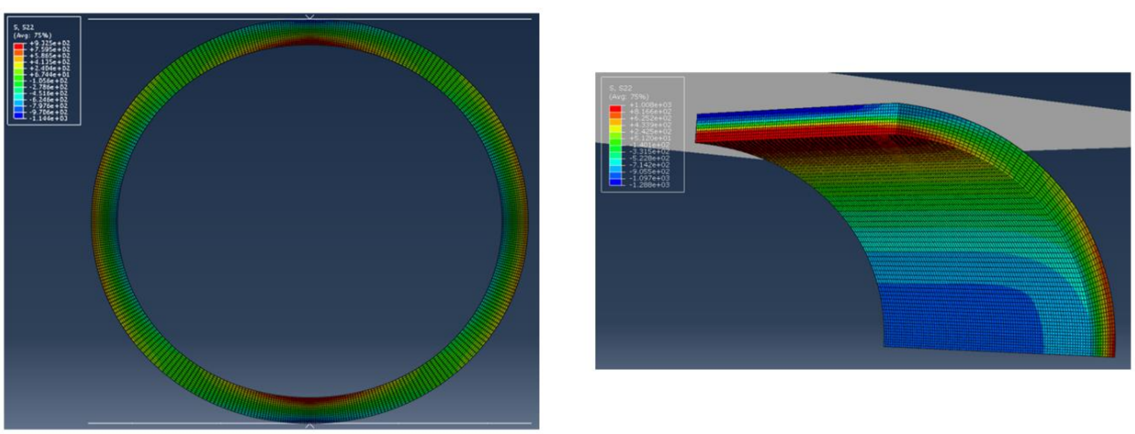

Figure 7. Images taken from Abaqus simulations with circumferential stress contours at low platen displacements. The 3D simulations employed symmetries at the 12 o’clock, 3 o’clock, and axial mid-length locations.

direction) were required to determine strain-hardening properties, and at least 14 elements through the wall-thickness (radial direction) were required to determine the failure strain. Similarly, for 3D simulations 8 through-wall thickness elements were acceptable for strain-hardening properties, but at least 10 elements through the wall thickness were required for failure strain determination. With these meshes the 2D quad elements had dimensions of 0.041 x 0.041 mm^2 at the 12, 3, 6, and 9 o'clock locations, and 0.041 x 0.122 mm^2 at the 1:30, 4:30, 7:30, and 10:30 o'clock locations. Similarly, the 3D meshes had dimensions of 0.057 x 0.057 x 0.057 mm^2 at the 12, 3, 6, and 9 o'clock locations and dimensions of 0.173 x 0.057 x 0.057 mm^2 at the 1:30, 4:30, 7:30 and 10:30 o'clock locations.

During simulations the steel platens were assumed to be rigid, as is common in other RCT simulation applications [4,6,7,17-24]. This is assumed to be acceptable because the RCT is dominated by bending, which produces small loads compared to material properties of steel. The contact coefficient between the platens and specimens was assumed to be 0.125 [6], but many studies have found that contact friction during RCT is negligible [18-20]. The mechanical properties were all assumed to be isotropic, and Poisson's ratio was defined as 0.37 [14]. Strain-rate dependence was not added to the material model to limit the parameter space. Therefore, the strain-rate experienced by the experimental RCT was effectively the reference strain rate. Displacement rates for the experimental RCTs were slow, so little variance is expected. However, transposing

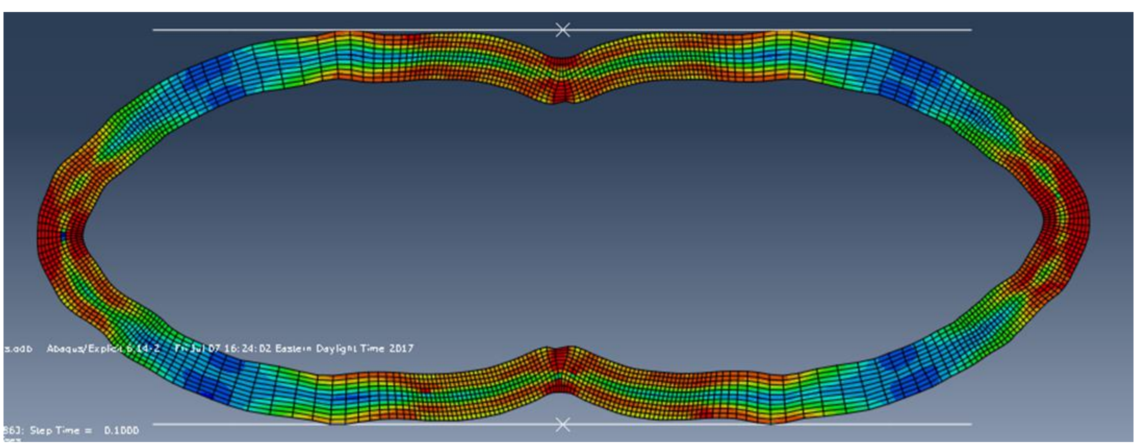

Figure 8. 2D simulation result showing unrealistic wavy effects that were fixed with the double precision and full nodal output options in the job editor.

properties determined with one displacement rate to a different displacement rate is not advised until future work explores its role.

3.3 Determining Mechanical Properties

The process for obtaining material properties was separated into 3 zones based on material behavior as shown in figure 9. The mechanical response of the specimen within each zone depends on varying parameters. Specifically, the mechanical response in zone I is dominated by Young's Modulus and yield stress, zone II is dominated by strain-hardening parameters, and zone III is dominated by the damage criterion.

3.3.1 Zone I

The method to calculate yield stress from experimental RCT data is shown in equation 1 below

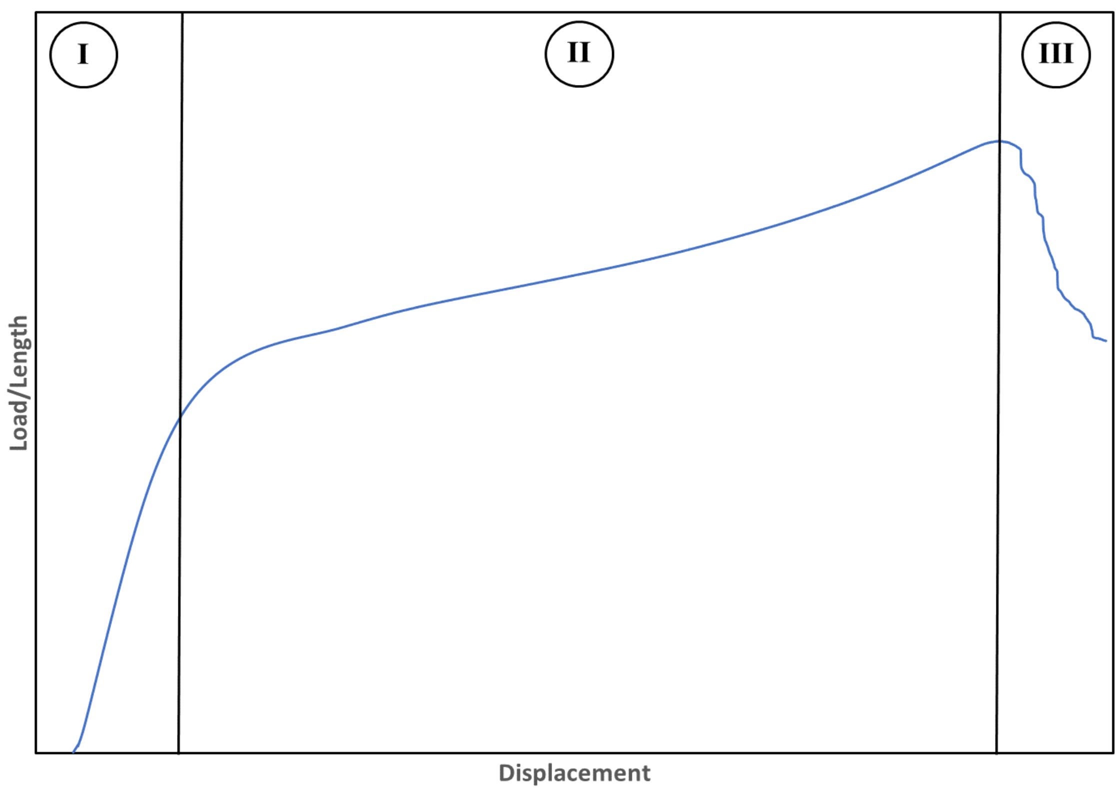

Figure 9. RCT result split into the 3 zones based on which mechanical properties dominate the response in that zone.

$$\sigma_0 = \frac{\alpha P_c R}{t^2 l} \qquad (4)$$

where α is a geometric constant = 0.866 since lengths were larger than the OD of the tubes, P_c is the collapse load obtained from figure 10 taken from [21], and R, t, and l are the radius, thickness and length of the tube respectively. This method was originally developed by Reddy and Reid [18-20]. The method to calculate Young's Modulus from experimental RCT data is shown in equation 2 below

$$E = \frac{12 P_e R^3 (1-\upsilon^2)}{\delta_e t^3 l}\left(\frac{\pi}{4} - \frac{2}{\pi}\right) \qquad (5)$$

where P_e and δ_e are the elastic load and deflection obtained from figure 10 from [21]. υ is Poisson's ratio, which was taken as 0.37 in this work [14]. This method was originally developed by Deruntz and Hodge [33]. These methods have been used in multiple studies, so they will not be discussed in detail here [4,6,18-24]. Their methods require the sample lengths to be greater than or equal to their OD to create plane strain conditions at their mid-length. For this purpose, rings were sectioned to 10mm lengths.

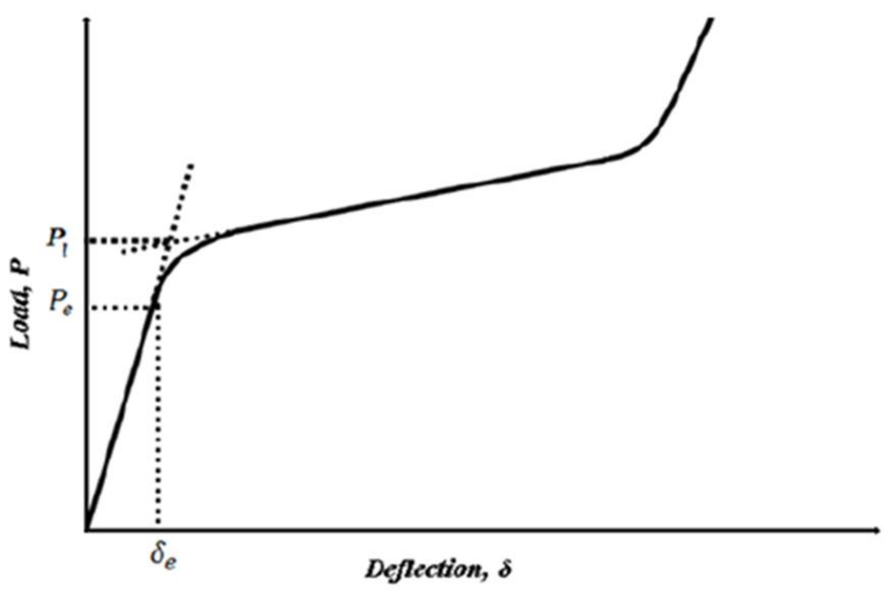

Figure 10. Plot taken from Nemat-Alla [21] showing how to obtain collapse load, elastic load, and elastic displacement.

3.3.2 Zone II

Similar to what was done in previous works [4,6,18-24], the best-fit coefficient, K, and exponent, n, for the Holloman relation, shown in equation 3, for zone 2 were found through empirical fitting.

$$\sigma = K\varepsilon^n \qquad (6)$$

This was done by first solving equation 4 below

$$\sigma_0 = K\varepsilon_0^n \qquad (7)$$

to solve for the elastic limit strain, ε_o, with the yield stress and estimated coefficient and exponent. The Holloman equation with the elastic limit strain is again manipulated into equation 5 below

$$\sigma = K\left(\varepsilon_0 + \varepsilon_p\right)^n \qquad (8)$$

with a linearly spaced vector of stress values (increments of 10 MPa in this work) to output corresponding values for ε_p, starting with $\sigma = \sigma_0$ and $\varepsilon_p = 0$. The produced stress vs plastic strain table was input into the Abaqus material definition, and the simulation was performed. Comparisons between that simulation and the experimental data dictated the next estimates for the Holloman coefficient and exponent, and the process was repeated until the simulations matched the experimental data up to failure.

3.3.3 Zone III

Material damage was modeled with the "damage initiation for ductile metals" material definition in Abaqus. This material definition is a phenomenological Gurson-based model that estimates material damage by assuming that the equivalent plastic strain at damage initiation is a function of stress triaxiality and strain rate [41] and after damage has initiated a fracture energy is required until the element completely loses load-carrying capability. A general mechanical response taken from Abaqus documentation with the addition of the damage model is shown in figure 11 [41].

The ductile damage model requires inputs for four properties: ST, plastic strain (εp-fail), strain rate, and fracture energy. ST is the ratio of mean stress to the von Mises stress. The plastic strain is specifically the plastic strain at the onset of damage. The fracture energy is descriptive of the internal work that an element can undergo until it breaks. After breaking, the element was deleted in the model, thus creating a crack. With this element deletion feature, the possibility of fracture testing is also investigated.

The ST and plastic strain during the onset of damage at the failure location were directly exported from simulations after zone 1 and 2 properties were determined. More description is given in the results section. Since no equivalent plastic-strain vs ST properties could be found in the literature for Zirconium-based alloys, data for aluminum from Hooputra [37] shown in figure 12 was used as a guide. Specifically, their results showed an exponential increase in plastic strain at failure as ST decreased from 1 to 0, so a linear increase in plastic strain was expected to be acceptable if not conservative. Higher fracture strains 10 and 0.5, were used at compressive ST, -0.6 and 0, respectively. These values were used to add continuity to the damage definition but also ensure that the model does not undergo unrealistic void-based damage at compressive stress states.

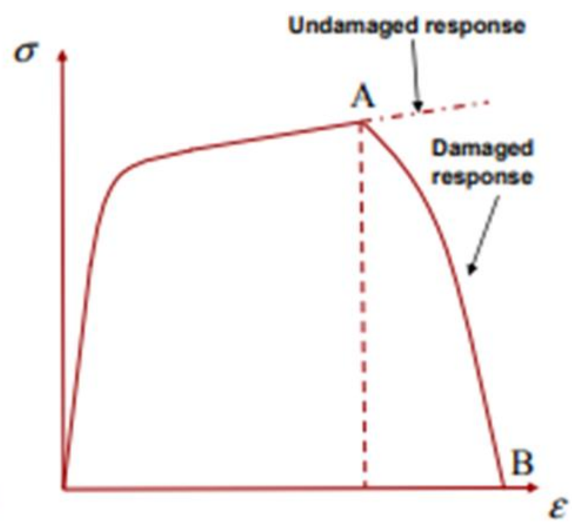

Figure 11. General mechanical response from Abaqus [41] showing damage initiation at A and complete loss of load-carrying capability at B when the phenomenological Gurson-based model is implemented

Fracture energy, which dictates the work required for a surface to advance from damage onset to loss of load-carrying capability, is a necessary variable to apply the Gurson-based model. This variable was found through empirical fitting by matching the slope of the experimental RCT response after failure initiation to the slope of the simulation RCT after failure initiation. The load-loss progression was chosen to be linear to limit the parameter space.

Strain-rate dependence was not included in the material model, implying that the experimental strain rate is the reference strain rate. The damage definition requires an input, however, so the experimental displacement rate was used. To clarify, this paper is not claiming that the displacement rate can be generally substituted for the strain rate, but that the material model in simulations did not account for strain rate dependence. Displacement rates for the experimental RCTs were slow, so little variance is expected. However, transposing properties determined with one displacement rate to a different displacement rate is not advised until future work explores its role. An example of the material damage input used in this work is shown in figure 13.

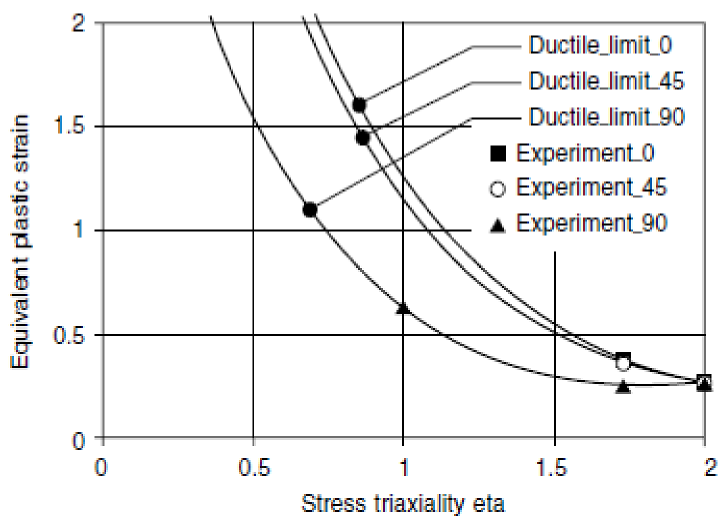

Figure 12. ε^p_{eq} vs ST response of Aluminium from Hooputra [37] that guided the ductile damage properties used in this work. Of note is the exponential increase in ε^p_{eq} as ST decreases from 0.57 to 0. In this work, ε^p_{eq} is assumed to increase linearly as ST decreases from 0.57 to 0, which is expected to be conservative.

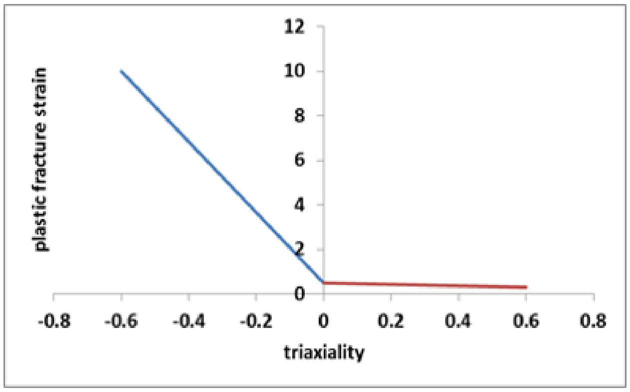

	Fracture Strain	Stress Triaxiality	Strain Rate
1	10	-0.6	0.0333
2	0.5	0	0.0333
3	Ep-fail	ST	0.0333

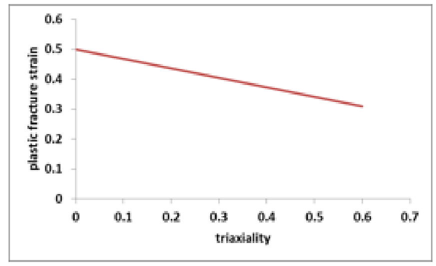

Figure 13. The ε^{p}_{eq} vs ST response that was used in this work for Zry-4 material. The tabular data shows the direct inputs from simulation results. The plots show this response for as-received Zry-4 obtained from this procedure.

4 RESULTS

4.1 Experimental

4.1.1 Experimental RCTs with AR Zry-4

Experimental data from RCTs performed at room temperature with different-length as-received Zry-4 tubes are shown in figure 14 where the load is normalized by each specimen's length, and the displacement refers to the top platen displacement.

As-received Zry-4 cladding tubes exhibited high ductility showing no signs of damage until 5 to ~5.5mm displacement. Material damage was apparent from load-displacement behavior, and post-test examinations of the sample revealed visible cracks on the sample surface in the OD 3'oclock position. These results show a strong length-

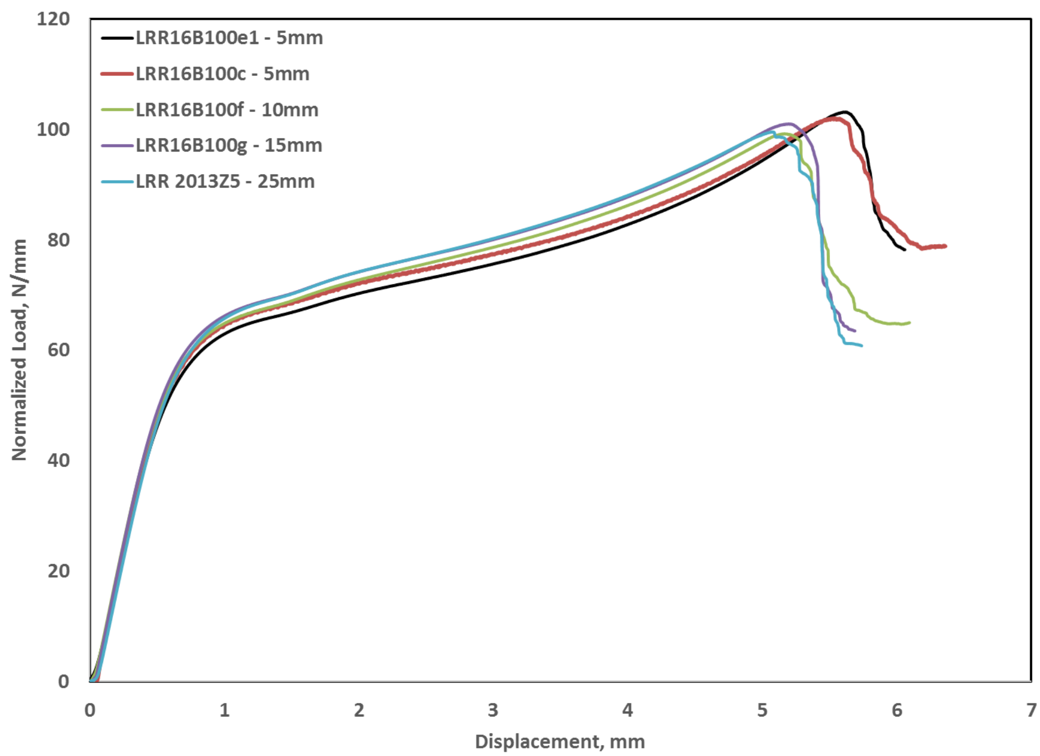

Figure 14. Experimental results of as-received Zry-4 RCTs of varied lengths. Importantly, failure strain was not shown to be sensitive to specimen length as long as the length was greater than the OD. However, fracture energy, shown by the slope of the load-loss portion, appeared to be sensitive to specimen length even at lengths greater than the OD.

dependence of the displacement at failure of RCT specimens when the length was less than the OD, but the displacement at failure was less sensitive at lengths greater than the OD. This was expected based on Reddy's result that the stress state changes at smaller lengths [18-20]. Fracture energy for crack propagation is still highly dependent on sample length however, even at lengths greater than the OD.

4.1.2 Experimental RCTs with hydride Zry-4

Experimental data from RCTs with hydrided Zry-4 specimens are shown in figure 15. It was observed that as hydrogen concentrations increased, the specimens showed significant loss of ductility as expected [1-6,14]. The most obvious sign of embrittlement was the consistent decrease in the displacement at failure and the rate of load-loss after failure initiation as hydrogen contents increased.

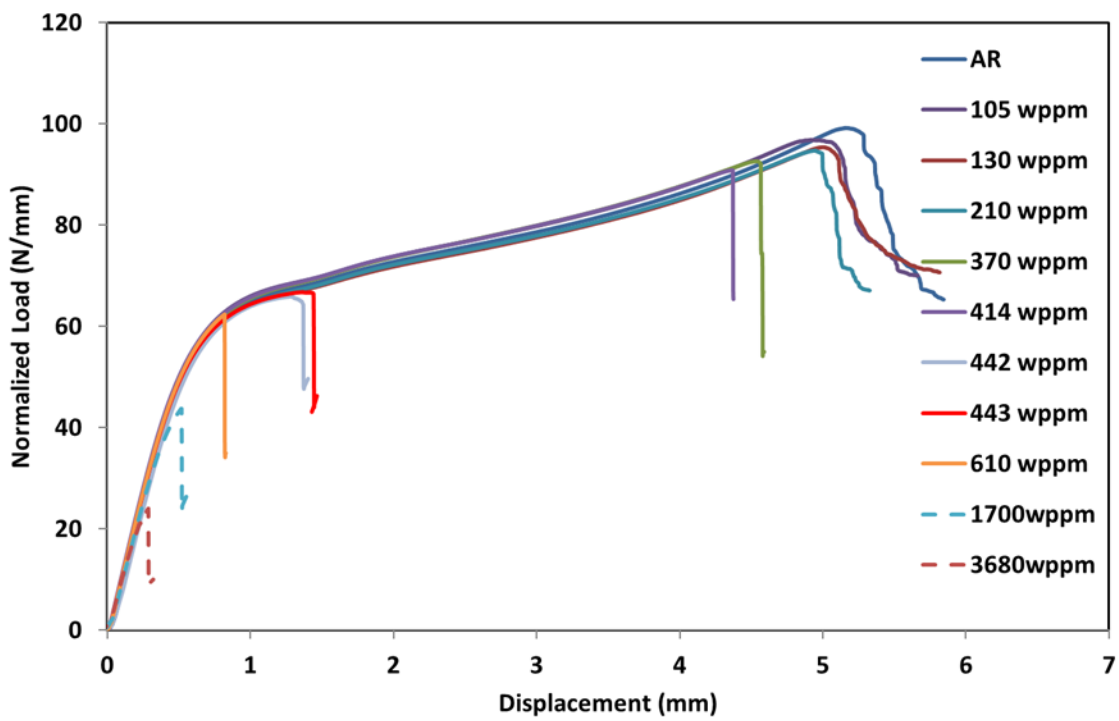

Figure 15. Experimental results of RCTs with Zry-4 with varied hydrogen concentrations. The embrittlement of hydrided Zry-4 is apparent as the displacement at failure decreases as hydrogen concentrations increase. The 1700 and 3680wppm specimens were 5mm long so their response is accompanied with some error. They were included in this figure for completeness, but they were not analyzed with the other specimens.

Post-test examinations of samples with higher hydrogen contents revealed obvious cracks, most of the time through an entire wall thickness and axial length in at least one location. Specimens that failed at displacements above ~2.7mm failed at the 3 o'clock position, 9 o'clock position, or both, and specimens that failed below ~1.5 mm failed at the 12 o'clock position, 6 o'clock position, or both. The experimental results revealed a large gap between the displacements at failure when the hydrogen concentration increased from 414 to 442 wppm, which is similar to the behavior of other work's hydrided Zry-4 datasets [4].

4.2 Computational

4.2.1 Simulations and mechanical properties for Zones 1 & 2

The mechanical properties determined for each hydrogen concentration are shown in table 2. The mechanical properties in plot form are shown in the discussion section. The Young's Moduli from experimental RCT data were calculated with reasonable accuracy with respect to expected values from the literature [14,42]. Similarly, the final

Table 4. Mechanical properties for zones I and II obtained with the process in this work for 2D plane-strain and 3D models.

	2D				3D			
H content	E (GPa)	σ_{ys} (MPa)	K	n	E (GPa)	σ_{ys} (MPa)	K	n
AR	89	790	1100	0.09	89	820	1125	0.09
105	90	800	1125	0.09	90	820	1125	0.09
130	92	780	1100	0.09	92	820	1100	0.09
210	90	780	1100	0.09	90	820	1100	0.09
370	92	790	1125	0.09	92	820	1150	0.09
414	92	790	1125	0.09	92	820	1150	0.09
442	87	790	1090	0.09	87	820	1100	0.09
443	87	780	1090	0.09	87	820	1110	0.09
610	87	790	1090	0.09	90	820	1110	0.09

strain-hardening properties were close to expected results [43]. Yield stresses, however, were consistently calculated to be 780-820MPa, which is slightly higher than values measured from conventional testing [14,42] but is consistent with other works' calculations from RCTs [4].

Figure 16 below shows an example of simulations before failure definition that were matched to experimental results. It was clear that . An exceptional fit was achieved for zones 1 & 2.

4.2.2 Final simulations results and Mechanical properties for zone 3

After zones 1 & 2 were matched to experimental results, the triaxiality and plastic strain at the displacement where the experimental and simulation results diverge are exported from the simulation. These two are used as the ST and $\varepsilon_{p\text{-fail}}$ input parameters for the damage model. Figure 17 depicts this process.

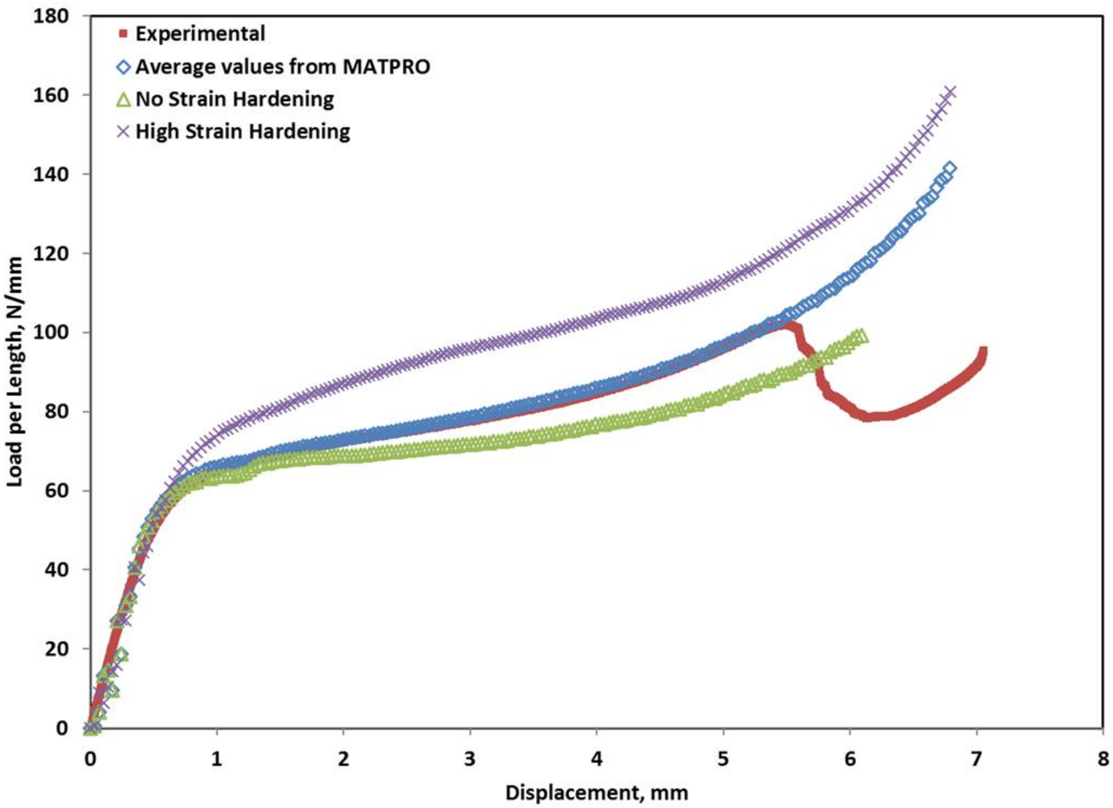

Figure 16. Load-displacement response of simulated RCTs with varied strain-hardening properties compared to experimental as-received specimen. A good match was found for zones I and II above (blue markers).

Final matched RCT results from this method are shown in Figure 18. As shown by these results, the experimental RCT of samples > 10mm length were matched well by simulations including the fracture region in 2D and 3D. After completing a 3D simulation with the properties found in 2D plane strain, small differences were seen in the predicted load (~5% difference) and predicted displacement at failure (~3%). Despite the small size of these discrepancies, the parameters in 3D simulations were altered from those found in 2D simulations to match 3D simulations to experimental results. The plot in figure 13a shows the original 3D simulation with 2D parameters as well as the 3D

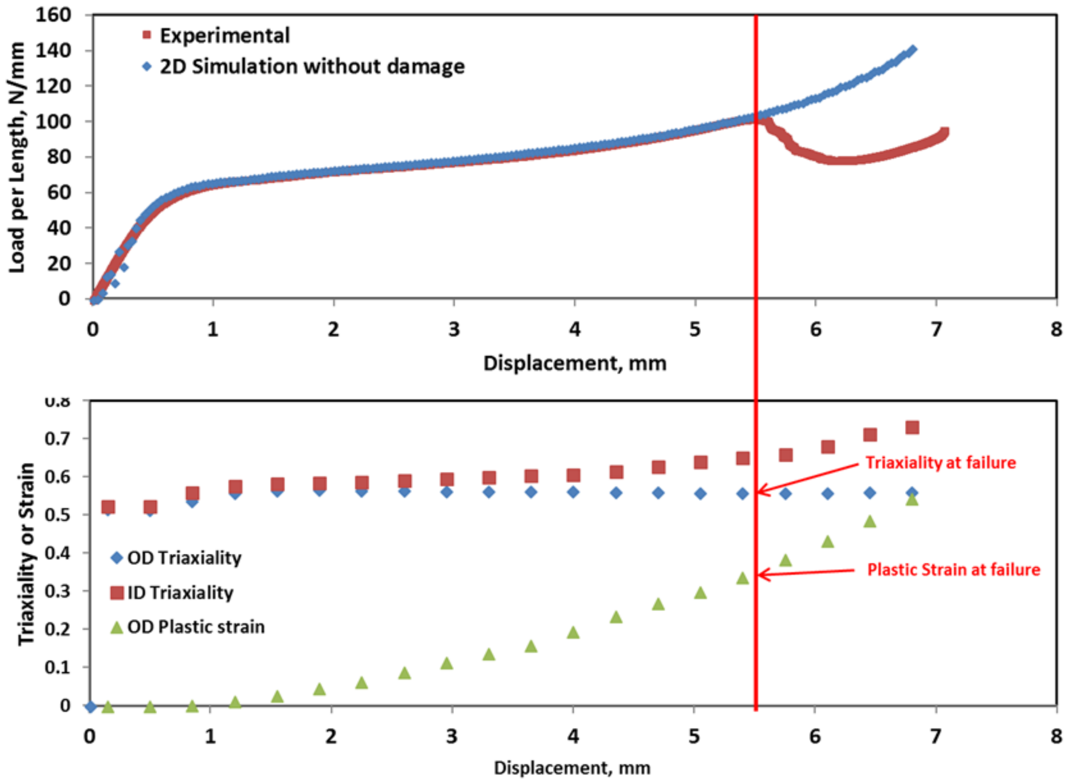

Figure 17. The process to obtain ε^p_{eq} and ST from simulation results by empirically fitting zone 1 and 2 simulation to those of experimental results then exporting the plastic strain and triaxiality from the simulation.

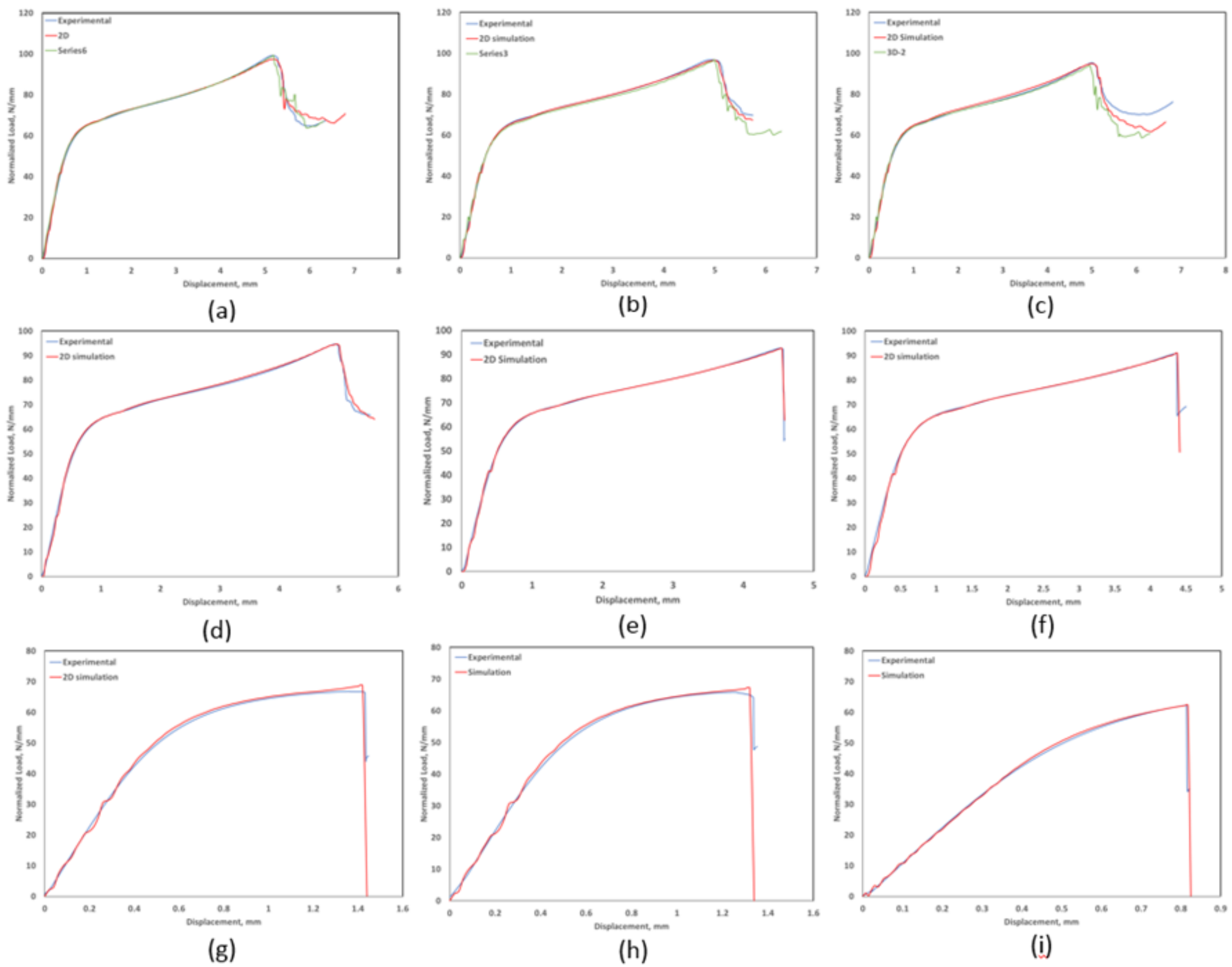

Figure 18. Overall results of matching Abaqus simulations with the Gurson-based model to the experimental results of specimens with varied hydrogen concentrations. Hydrogen concentrations in wppm are as follows: (a) AR (b) 105 (c) 130 (d) 210 (e) 370 (f) 414 (g) 442 (h) 443 (i) 610. Exceptional fits were achieved.

simulation with updated parameters. The rest of the plots show only the updated parameters for visibility. From the plots it was apparent that the 2D simulations slightly underpredicted the plastic strain at failure, but they overpredicted fracture energy relative to their 3D simulation counterpart.

The properties determined for the damage model for each hydrogen concentration specimen by this method are shown in table 5. The mechanical properties are shown in plot form in the discussion section. The results in the "2D" columns were parameters determined from 2D simulations, and in the "3D" columns were found from updated 3D simulation-experimental matching. The differences in damage parameters from 2D vs 3D are apparent but acceptable for plastic strain at failure. For fracture energy, differences between 2D and 3D simulations were more significant. The clear trend representing decreasing plastic strain at fracture and fracture energy with increasing hydrogen contents was apparent for both simulation types.

Table 5. Mechanical properties for the Gurson-based damage model used in this work.

	2D		3D	
H content	ε_{frac}	Frac. Energy	ε_{frac}	Frac. Energy
AR	0.28	5	0.32	1
105	0.255	5	0.3	1
130	0.25	5	0.31	1
210	0.26	4	0.3	0.8
370	0.25	1	0.22	0.01
414	0.235	0.5	0.2	0.01
442	0.084	0.5	0.065	0.01
443	0.08	0.5	0.065	0.01
610	0.035	0.1	0.015	0.01

4.2.3 Observation of RCT phenomena

Figure 19 shows 2D plane strain simulations where the effect of yield stress and strain-hardening on the cross-sectional shape of RCTs at high displacements was demonstrated. Based on experimental works [4,18-20], the ring is expected to separate from the platens at the 6 o'clock and 12 o'clock positions. Since the simulation without yield does not separate, but those with plasticity do separate, this phenomenon is concluded to be a consequence of ring yielding. Furthermore, it was observed that strain-hardening reduces the curvature of the RCT specimen cross-section.

Moreover, anticlastic bending that was first reported by Reddy and Reid [18-20] was observed in 3D simulations. Specifically, bending at the 3 and 9 o'clock ID positions at the specimen ends was exhibited and was expected to be caused by the high compressive stresses at the 3 and 9 o'clock ID mid-length locations. Additionally, anticlastic curvature was observed at the 12 and 6 o'clock locations.

An analysis on the load increase for the elastic, perfectly-plastic (yield stress, no strain hardening) simulation was also performed. It was observed, consistent with Reddy and Reid's [18-20] discussion, that this load increase was due to a decrease in the bending moment arm at higher displacements as the RCT specimen dog-bones, moving the ring-plate contact point. Figure 20 depicts this phenomenon.

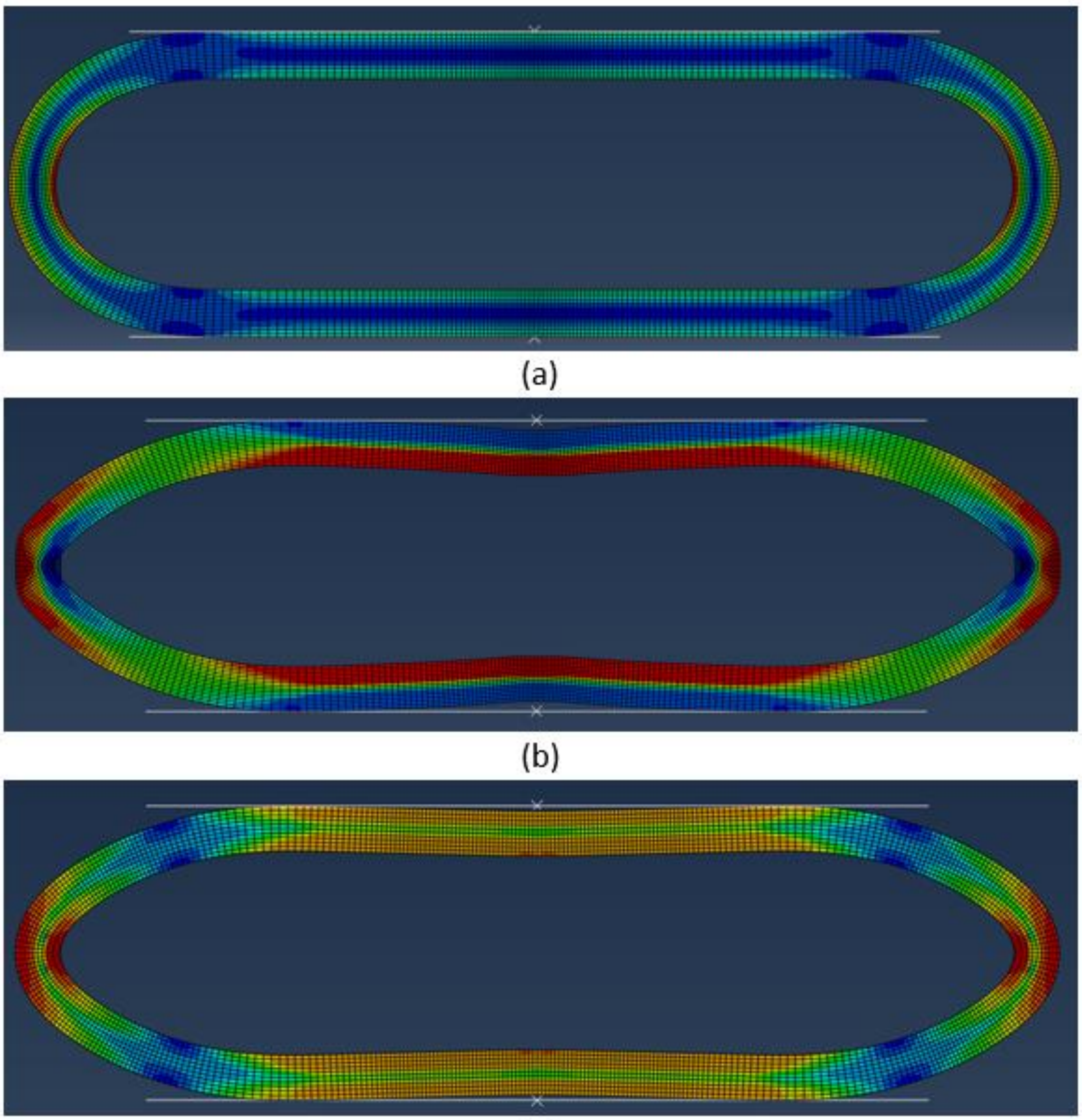

(a)

(b)

(c)

Figure 19. 2D simulations with (a) only elasticity, (b) elastic-perfectly plastic, and (c) Holloman relation strain-hardening response demonstrating the geometry sensitivity of RCT rings to plasticity properties.

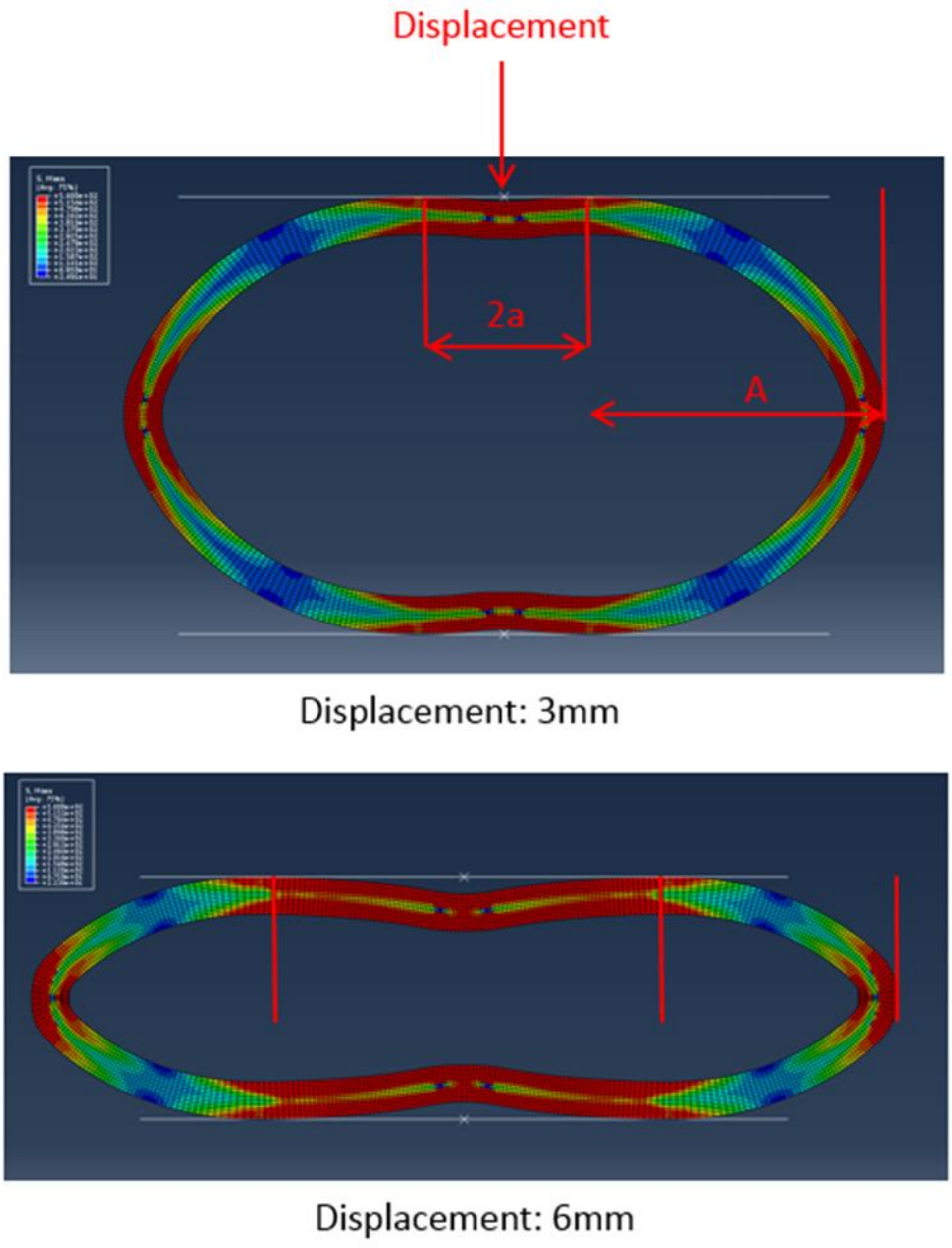

Figure 20. Simulation result with an elastic-perfectly plastic material model. As platen displacement increases, ring deformation results in movement of the contact point that decreases the moment-arm, A. This reduction in moment arm length causes the load to increase as platen displacement increases.

5 DISCUSSION AND FUTURE WORK

5.1 Discussion

5.1.1 Length Dependence

Based on experimental RCT results with different-length as-received Zry-4 specimens shown in figure 13, displacement at failure is not significantly sensitive to specimen length provided the specimen is longer than its OD, although small discrepancies were observed. These discrepancies were mainly attributed to geometric differences between the Zry-4 tubes versus those analyzed by Reddy and Reid. Specifically, the tubes used in this work were slightly thick-walled (diameter to thickness ratio was 18) whereas the tubes analyzed by Reid and Reddy were thin-walled (diameter to thickness ratio ranged from 28 to 50). The main distinction between thin- or thick-walled shells is the more substantial radial-direction strains with thick-walled shells. Further, some of the discrepancies were attributed to mechanical property specimen geometry tolerances shown by the small variance in mechanical response between same-length samples.

Fracture energy determination, however, was clearly sensitive to sample length, even at lengths greater than the OD. This is mostly because as the crack propagates in the axial direction toward the specimen ends, the stress state near the crack front changes to that closer to plane stress. Crucially, cracks on shorter-length samples will encroach on the specimen ends before longer-length samples. Additionally, the lack of mesh refinement, crack-tip properties, true axial-direction properties, and metal matrix-hydride separation mechanics may have introduced errors in the crack propagation properties from these analyses.

Although the differences between 10mm and longer-length specimens were small except for the fracture energy, they were found to be real. This explains the differences in 3D simulations when they were run with the parameters determined from 2D simulations. Future work with longer-length specimens would be required to verify that the differences between 2D and 3D simulations disappear when fitting 2D properties to longer samples. Fracture energy would require at least significantly longer samples, and potentially fracture mechanics modeling techniques.

5.1.2 Large Displacement-at-Failure gap between 414 and 442 wppm

From the experimental results with hydrided Zry-4, a large jump in displacement at failure was observed between 414 and 442 wppm. The primary reason this gap is so large is because a hinge is developed at the 6 and 12 o'clock ID locations after 1.5mm displacement [18]. To demonstrate, Figure 21 shows the plastic strain at the mid-length 12 o'clock ID and mid-length 3 o'clock OD positions. After 1.5mm of displacement, the 12 o'clock location of the ring flattens, so any further deformation results in hinge displacement instead of further strain at this location. Additionally, plastic strains at the 3 o'clock OD position do not surpass the plastic strain at the 12 o'clock location until roughly 2.7mm platen displacement, meaning deformation during these platen displacements does not produce more severe local damage. This suggests that if failure has not been initiated by 1.5mm, it will not fail until 2.7mm or greater displacements.

5.1.3 Mechanical Properties

It is important to note that tests with new nuclear materials or those exposed to complex nuclear environments may not have reported comprehensive material properties to check results, so validating these methods for obtaining mechanical properties for known materials is crucial. This affects the outlook of these methods as a technique to gain mechanical properties for emerging materials. This becomes even more impactful considering the high costs required to setup and run more sophisticated mechanical property tests in hot cell environments.

One possible explanation for the difference in Zry-4 yield stress compared to reported values could be that the outer diameter to wall thickness ratio (D/t) of the Zry-4 tubes was slightly larger than the tubes tested by Reddy and Reid. Specifically, the tubes tested by Reddy and Reid are unquestionably thin-walled shells, whereas the Zry-4 tubes are slightly thick-walled meaning that radial-direction deformations are more significant. For reference, a structure is deemed thin-walled if $D/t > 20$, and thick-walled otherwise.

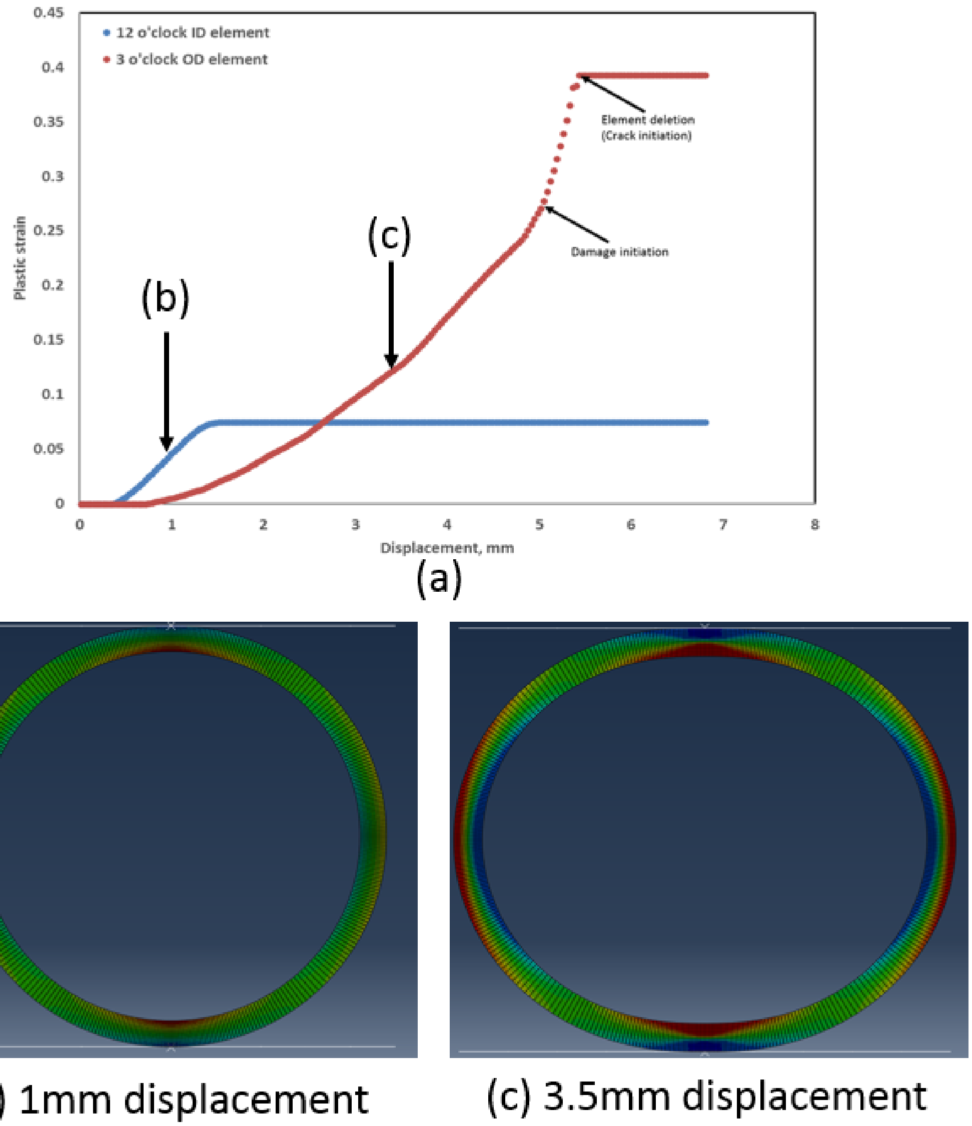

Figure 21. (a) The plastic strain vs. displacement of a ring explaining the large gap at failure between 414 and 443 wppm specimens. The plastic strain at the 12 o'clock ID location reaches a maximum when a traveling hinge is formed there. Further displacement results in displacement of the hinge instead of plastic strain at that location. The 3 o'clock OD location does not reach that plastic strain maximum until ~2.7mm. **(b) (c)** Images of 2D simulations at 1mm and 3.5 mm with circumferential stress contour showing the 12 o'clock ID maximum at low displacements and the 3 o'clock OD maximum at higher displacmeents.

Regardless of the mechanics, simulations with calculated Zry-4 properties matched up well suggesting that the calculations for those properties was acceptable.

The zone I and II mechanical properties determined for each hydrogen concentration shown in table 2 were calculated through previous authors' methods. Figure 22 below shows the zone I properties obtained from this method. The Young's moduli found in this work for different hydrogen concentrations was found to be consistent with the properties from literature [14,42,43] and insensitive to hydrogen contents like what is reported in the literature [4]. The yield stresses obtained from this work are slightly higher than the yield stresses obtained from other mechanical testing methods [14,42,43], but they were consistent with other works to obtain yield stresses from RCTs [4]. Further, they were found to be insensitive to hydrogen contents up to

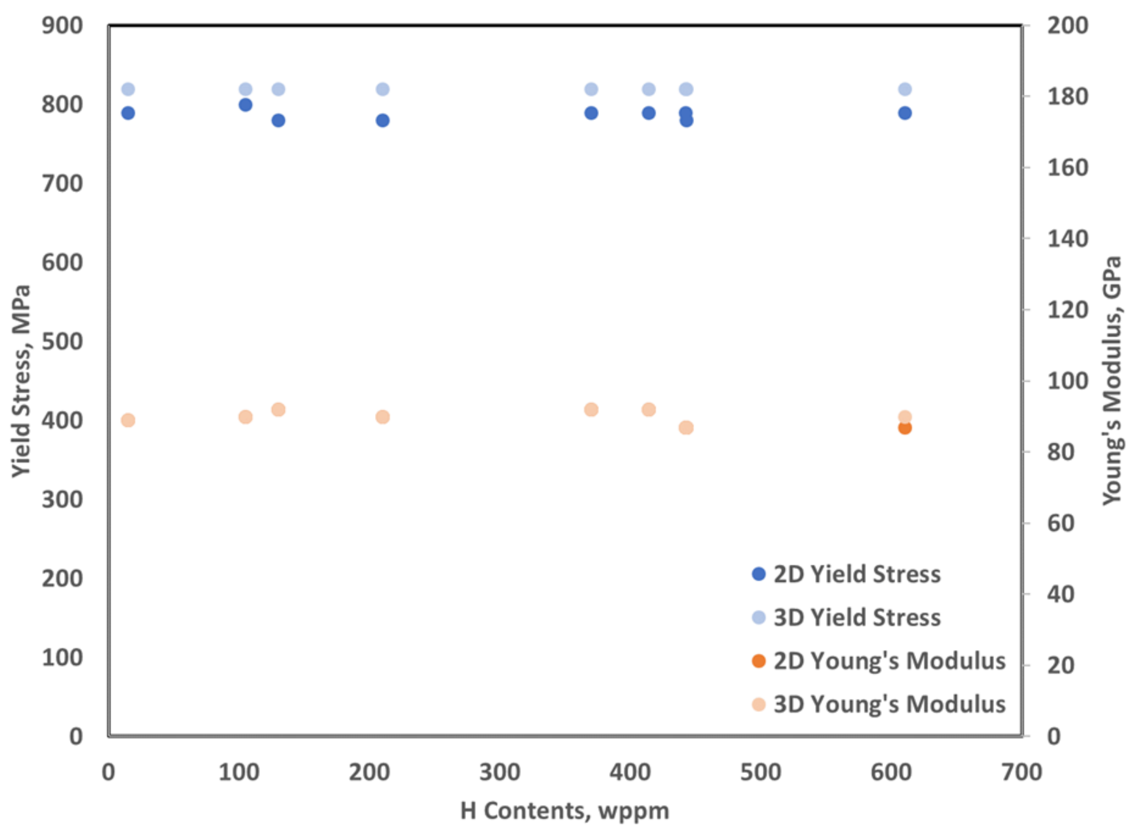

Figure 22. The zone I properties calculated with the methods developed by Reddy and Ried [18-20] and Deruntz and Hodge [33]. Young's Moduli were calculated to the same value as those found in the literature [14,42], and Yield Stresses were calculated to be similar to other work's calculations from RCT specimens. Both properties were observed to be insensitive to hydrogen concentrations up to 600 wppm.

600wppm, which is also reported in the literature [4]. Some of the discrepancy in calculated yield stresses with Reddy and Reid's method to conventional tests was attributed to the slightly thick-walled geometry of the Zry-4 tubes or from Zry-4 anisotropy, both of which were not factors for Reddy and Reid's material [18-20]. Regardless of the mechanics, simulations with the slightly over-calculated yield stress of Zry-4 with the isotropic assumption match with experimental results, suggesting that they are acceptable. Figure 23 shows the zone II properties obtained from this work. Strain-hardening values were consistent with those reported by MATPRO for the as-received condition [43]. In this work, strain-hardening properties were found to be insensitive to hydrogen concentrations up to 600 wppm. Other works did not report strain-hardening sensitivity to hydrogen concentrations up to 600 wppm; however, they also did not show data explicitly displaying that it was insensitive. Moreover, experimental RCT results of higher hydrogen contents stacked on top of other experimental results for zones 1 and 2 in this work and others [4].

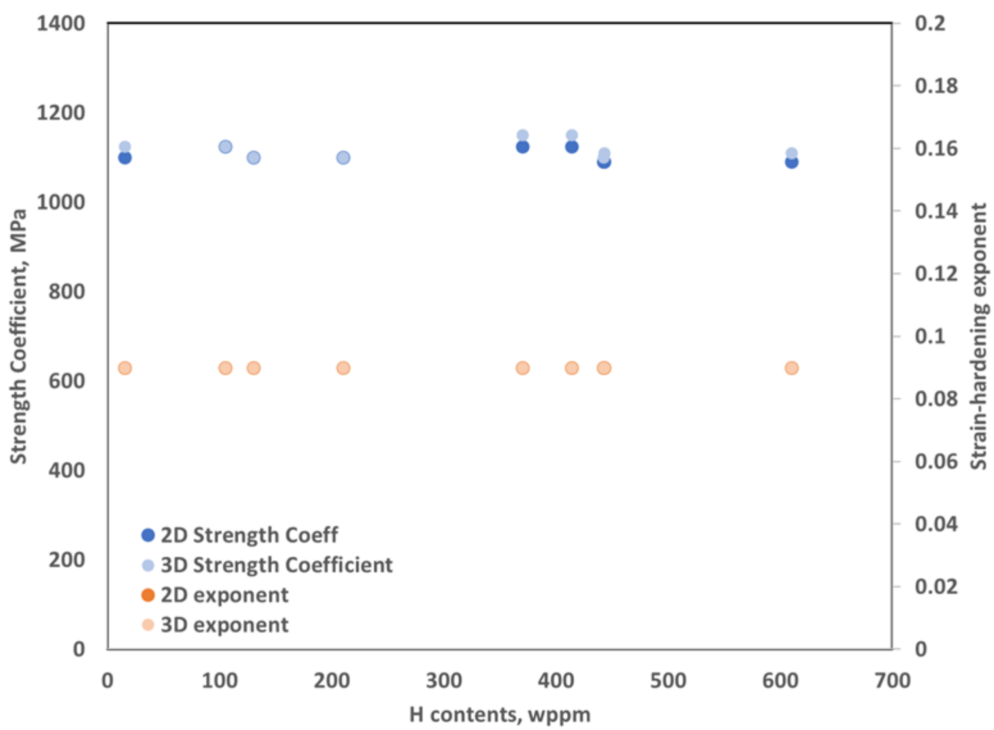

Figure 23. The zone II properties obtained by empirically fitting RCT simulations to experimental results using a Holloman relation. Both Holloman relation parameters were determined to be insensitive to hydrogen concentrations up to 600 wppm.

Figure 24 shows the plastic strain at failure determined from this work. It was observed that as hydrogen contents increased to 600wppm, the plastic strain at failure decreased as expected. There were some discrepancies (~10%) between plastic strain values determined from 2D and 3D simulations. These discrepancies were mostly attributed to be from the yield stress and strain-hardening property discrepancies from length-dependence. If a computer algorithm were developed to match the zone 1 and zone 2 properties exactly, then discrepancies between 2D and 3D plastic strains are expected to decrease. Le Saux et al. [5] reported hoop strains at failure between 0.55 and 0.75 for as-received Zry-4 material from hoop tension and expansion due to compression tests. Those tests would produce a different stress state at the failure location, which by the damage model, would imply that the plastic strain at failure should not be expected to be the same. Furthermore, Desquines et al [7] reported failure strains of Zry-4 sheet

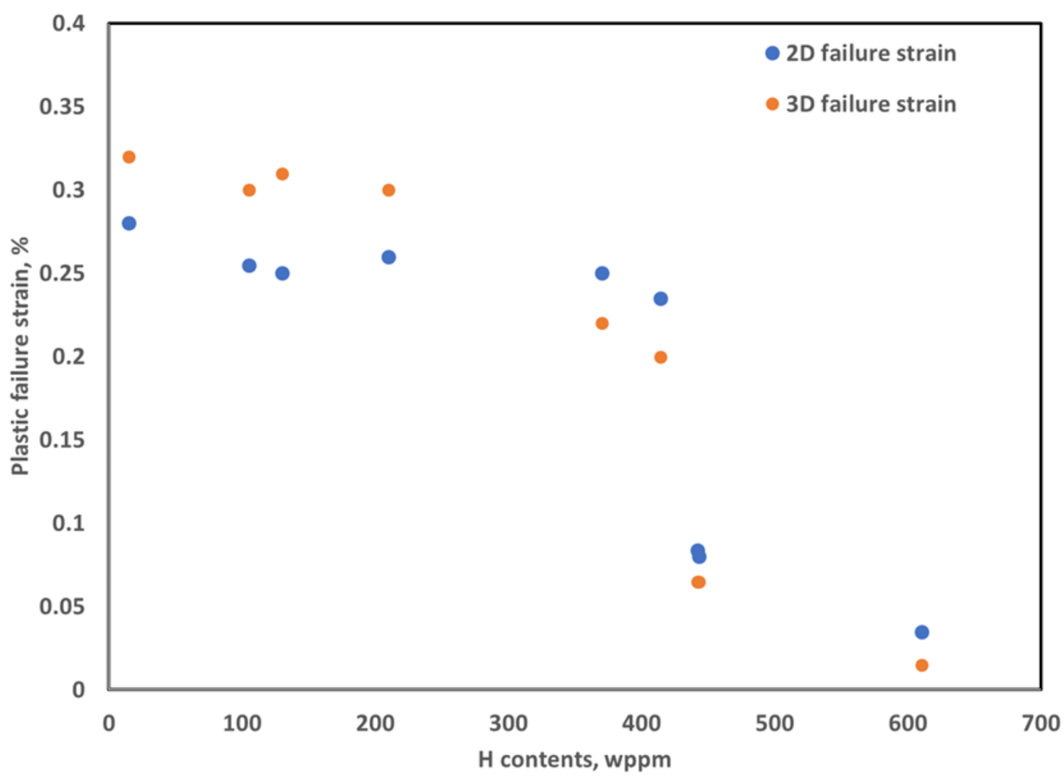

Figure 24. Plastic strain at fracture determined for the Gurson-based damage model from computational simulations. Failure strains between 2D and 3D simulations were within acceptable margins implying that both simulation types are acceptable to determine this mechanical property. A clear decreasing trend in plastic strain at fracture can be seen as hydrogen contents increase, showing the effect of hydrides on cladding ductility

material to be 0.15 wppm for as-received conditions tested in plane strain. Discrepancies between their result and those reported in this work are expected to be from the tube-forming processes that their Zry-4 sheet did not undergo. Regardless of the cause of the discrepancies, the plastic strain values obtained by this method are within acceptable margins with their results. Based on the results of this study, this method appears to be able to successfully recreate experimental RCT results and obtain plastic strain at failure from experimental RCTs provided the specimens are long enough. Using experimental data with slightly longer RCTs may provide slightly improved results, but it does not appear to be required for acceptable results.

Figure 25 shows the fracture energies obtained for Zry-4 tubes at different hydrogen contents obtained from this work. Similar to the failure strains, the fracture

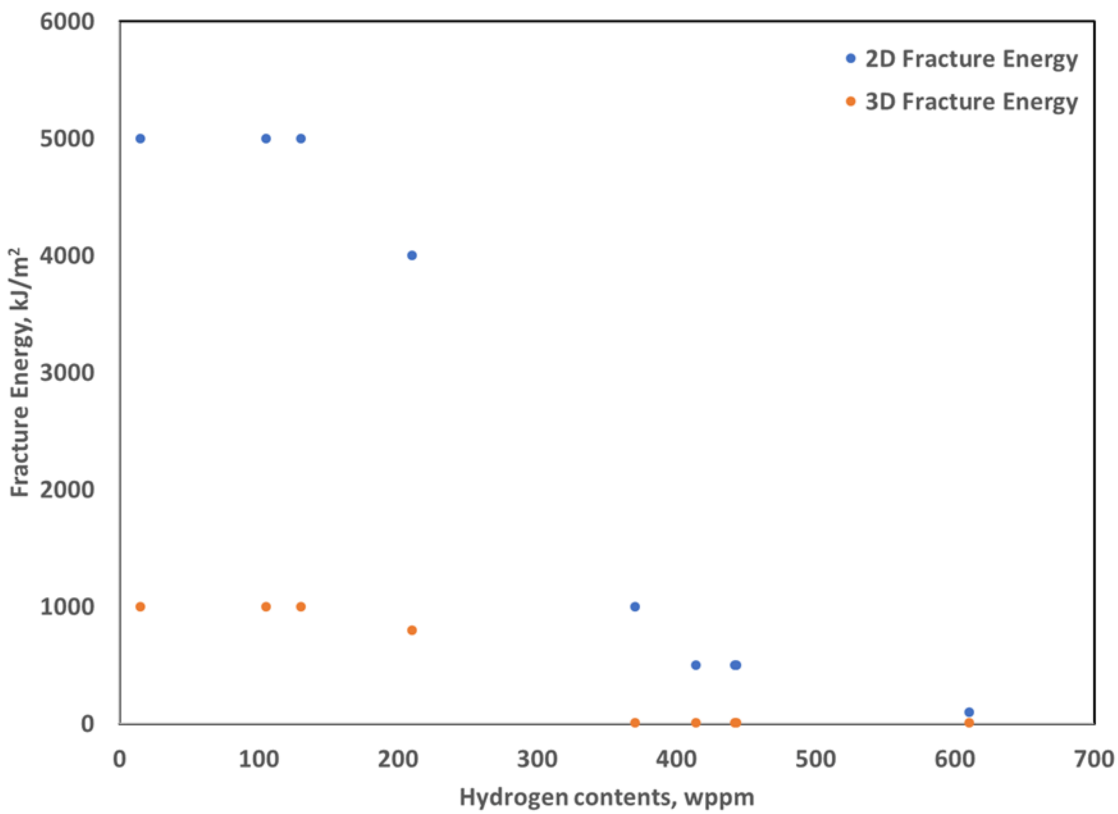

Figure 25. Fracture energies obtained for the Gurson-based model by empirical fitting from this work. Based on reported values from the literature, 3D simulations can determine fracture energy within acceptable margins; however, 2D simulations significantly overpredict the fracture energy. This is because the crack propagation in the axial direction causes the stress state at the crack front to change as it approaches the sample ends. 2D simulations cannot track changes in the axial direction.

energy obtained from 2D and 3D simulations decreased with increased hydrogen concentrations up to 600 wppm. A large gap between values obtained from 2D versus 3D models was observed. This gap was attributed to the 2D models' inability to replicate realistic stress states at the crack front as the crack moves in the axial direction. Specifically, 2D simulations can only model crack propagation in the radial direction. However, in experimental samples, the crack propagates in the axial direction toward the sample ends [6]. As the crack front approaches the sample ends, it is not in plane strain anymore, meaning the 2D simulations' plane strain assumption is no longer valid. Other errors associated with the fracture energy from a 10mm length sample could be attributed to the lack of fracture mechanics models and mesh refinement at the crack tip, but some error associated with length-dependence was also observed experimentally. Kim crudely calculated fracture energy by integrating force by displacement [4] and found that fracture energies range from 600 to ~10 KJ/m^2 as hydrogen contents ranged from as-received to 1050 wppm. Discrepancies between the results from this method and his results were expected due to the crudeness of Kim's calculation method. It was found that results from this new method were within an acceptable range of his results despite the difference in calculation methods.

5.2 Future suggestions

To properly obtain fracture energy, crack tip stress state changes in the axial direction are required unless experimental results are obtained from exceptionally long specimens, which is not possible for 2D simulations. Therefore, further investigation of this method as a crack estimation technique would need to include matching 3D simulations with metallography or DIC to confirm that experimental results match those of simulations. Using simulations for precise fracture energy results might require fracture mechanics techniques such as refined meshes at the crack tip and Extended Finite Element Method [44]. Furthermore, a more rigorous approach could include more complex modeling that includes hydride-matrix interface properties and hydride-hydride connectivity to better characterize the real crack path. Despite the lack of precise modeling techniques, fracture energies from this method could still serve as an estimation.

The damage model in this work is designed for use with void nucleation, growth, and coalescence, thus it is not designed to work for brittle specimens. However, since it is a phenomenological model, its applicability is possible for more brittle samples. If plastic deformation is low enough, specimens fail before the strain-hardening response begins, so the empirical fitting process to obtain those properties would be removed. Furthermore, the energy required to advance from failure initiation to crack initiation, the fracture energy input in ABAQUS, approaches zero, so arbitrarily low fracture energies that produce instant crack initiation at failure might be the only required parameter for the damage model. If this kind of work is attempted, fracture energy insensitivity would have to be validated. One major challenge with applying these methods to brittle specimens is when rings fail at relatively small displacements, there is not enough plastic deformation to calculate yield stresses with Reddy and Reid's equation.

Future work could involve 2D simulations to fit longer experimental tests or 3D fitting to investigate the technique's effectiveness in determining fracture energy. Those investigations could be further enhanced by using DIC to experimentally track strains or strain rates on the sample surface or post-test metallography showing the crack path. Another approach to determining more exact fracture energies could be to model hydride inclusions in the metal matrix by combining properties of the metal, hydrides, and hydride-metal interface, which would be much more involved.

Bizet et al added a probability density function to their material model for simulations fitted to experimental RCTs with aluminum to allow for heterogeneous yield strengths to account for material defects [24]. They found that adding these heterogenous effects to their material model performed better when material properties from one mechanical testing method are transposed to a simulation of another testing method. This approach could perhaps be applied with a probability density function for hydride-hydride connectivity based off of metallographic analysis of hydride density.

Since the shape of the ring cross-section during RCTs is highly sensitive to yield stress and strain-hardening, simply imaging the shape of the experimental ring and comparing it to the shape during simulations could qualitatively determine the viability of the isotropic or other assumptions made in the model. Furthermore, this information could be used to inform anisotropic properties in attempts to obtain them from RCTs.

Perhaps the largest strength of the damage model is its ability to aggregate damage from different stress states, meaning it can include damage from loading history. This becomes especially crucial in the case of SNF transportation and storage, where the cladding tubes are susceptible to lateral compression, bending, axial tension, vibration. If the plastic strain vs triaxiality function can be filled out for at least the relevant stress states in transportation and storage, the model shows significant promise in being able to predict SNF safety. Challenges with creating this general definition include anisotropy, which are more difficult and expensive to obtain and would require a stress state definition that was direction dependent. Finally, incorporating fuel pellet and pellet-cladding bonding to mechanical response models would further improve failure prediction capabilities; however, that creates a significantly more complex structure with various mechanisms of failure.

6 CONCLUSIONS

This paper adds a Gurson-based ductile damage model to RCT simulations using an integrated approach with experimental RCTs to determine material properties of Zry-4 cladding specimens. Based on the results, 2D simulations can be implemented to obtain Young's modulus, yield stress, and strain-hardening parameters. Furthermore, they can match experimental RCT behavior including the fracture portion and determine plastic strain at fracture from 10mm ring specimens that does not require empirical fitting, but more precise strains could be determined from 3D simulations. Fracture energy, on the other hand, requires minimal empirical fitting with 2D simulations matched to experimental samples that are longer length or 3D fitting at any length, but even these improvements could only provide estimates unless they include fracture mechanics models and remeshing.

LIST OF REFERENCES

[1] Y. Yan, A. Blackwell, L. Plummer, B. Radhakrishnan, S. Gorti, K. Clarno. *Observation and Mechanism of Hydride in Zircaloy-4 and Local Hydride Reorientation Induced by High Pressure at High Temperatures.* International High-Level Radioactive Waste Management, Albequerque, NM, April 28 – May 2, (2013)
[2] Jun Hwan Kim, Myoung Ho Lee, Byoung Kwon Choi, Yong Hwan Jeong. *Effects of Oxide and Hydrogen on the Circumferential Mechanical Properties of Zircaloy-4 Cladding.* Nuc. Eng. And Design 236 (2006) 1867-1873.
[3] M. Le Saux, J. Besson, S. Carassou. *A Model to Describe the Mechanical Behavior and the Ductile Failure of Hydrided Zircaloy-4 Fuel Claddings between 25C and 480C.* J. of Nuc. Mat. 466 (2015) 43-55.
[4] Ju-Seong Kim, Tae-Hoon Kim, Dong-Hak Kook, Yong-Soo Kim. *Effects of Hydride Morphology on the Embrittlement of Zircaloy-4 Cladding.* J. of Nuc. Mat. 456 (2015) 235-245.
[5] H. C. Chu, S. K. Wu, R. C. Kuo. *Hydride Reorientation in Zircaloy-4 Cladding.* J. of Nuc. Mat. 373 (2008) 319-327.
[6] M.A. Martin-Rengel, F.J. Gómez Sánchez, J. Ruiz-Hervías, L. Caballero. *Determination of the Hoop Fracture Properties of Unirradiated Hydrogen-Charged Nuclear Fuel Cladding from Ring Compression Tests.* J. of Nuc. Mat. 436 (2013) 123-129.
[7] J. Desquines, D.A.Koss, A.T. Motta, B. Cazalis, M. Petit. *The Issue of Stress State during Mechanical Tests to Assess Cladding Performance during a Reactivity-Initiated Accident (RIA).* J. of Nuc. Mat. 412 (2011) 250-267.
[8] M.C. Billone, T.A. Burtseva, R.E. Einziger. *Ductile-to-Brittle Transition Temperature for High-Burnup Cladding Alloys Exposed to Simulated Drying-Storage Conditions.* J. of Nuc. Mat. 433 (2013) 431-448.
[9] Young-Jun Kim, Dong-Hak Kook, Tae-Hoon Kim, Ju-Seong Kim. *Stress and Temperature-Dependent Hydride Reorientation of Zircaloy-4 Cladding and its Effect on the Ductility Degredation.* J. of Nuc. Sci. and Tech. 52, No. 5 (2015) 717-727.
[10] K. Linga Murty, Indrajit Charit. *Texture Development and Anisotropic Deformation of Zircaloys*. Prog. In Nuc. En. 48 (2006) 325-359.
[11] C.R.F. Azevedo. *Selection of Fuel Cladding Material for Nuclear Fission Reactors.* Eng. Fail. Analysis (2011), doi:10.1016/j.engfailanal.2011.06.010
[12] Kurt. A. Terrani. *Accident Tolerant Fuel Cladding Development: Promise, Status, and Challenges.* J. of Nuc. Mat. 501 (2018) 13-30.
[13] NRC Standard Review Plan for Spent Fuel Dry Storage Systems at a General License Facility. NUREG-1536, Revision 1 (2010)
[14] Robert S. Daum, Saurin Majumdar, Michael C. Billone. *Experimental and Analytical Investigation of the Mechanical Behavior of High-Burnup Zircaloy-4 Fuel Cladding.* J. of ASTM Inter, Vol. 5, No. 5 (2008) Paper ID: JAI101209.
[15] B. Hanson, H. Alsaed, C. Stockman, D. Enos, R. Meyer, K. Sorenson. Used Fuel Disposition Campaign: Gap Analysis to Support Extended Storage of Used Nuclear Fuel. PNNL-20509 (2012)
[16] NRC Draft REGULATORY GUIDE DG-1262, *Testing for Post-Quench Ducitlity.* ML12284A325 (2014)

[17] Rayji Yamada, Motoe Suzuki, Yasuo Harayama. *Application of Finite Element Method to Ring Compression Test.* Nuc. Eng. And Des. 44 (1977) 75-85
[18] S. R. Reid, T. Yella Reddy. *Effect of Strain-Hardening on the Lateral Compression of Tubes between Rigid Plates.* Int. J. of Solids Structures 14 (1978) 213-225.
[19] T. Yella Reddy, S. R. Reid. *On Obtaining Material Properties from the Ring Compression Test.* Nuc. Eng. And Des. 52 (1979) 257-263
[20] T. Yella Reddy, S. R. Reid. *Phenomena Associated with the Crussing of Metal Tubes between Rigid Plates.* Int. J. Solids Structures 16 (1980) 545-562
[21] Mahmoud Nemat-Alla. *Reproducing Hoop Stress-Strain Behavior for Tubular Material Using Lateral Compression Test.* Int. J. Mech. Sci. 45 (2003) 605-621
[22] Gayan Rathnaweera, Yvonne Durandet, Dong Ruan, Shigeaki Kinoshita. *Characterizing the Material Properties of a Tube from a Lateral Compression Test.* Int. J. of Protective Struc. 2, No. 4 (2011) 465-475
[23] Daw-Kwei Leu. *Finite-Element Simulation of the Lateral Compression of Aluminum Tube between Rigid Plates.* Inter. J. of Mech. Sci. 41 (1999) 621-638
[24] Laurent Bizet, Ludovic Charleux, Pascale Balland, Laurent Tabourot. *Influence of Heterogeneities Introduced into the Modelling of a Ring Compression Test.* Archives of Civ. And Mech. Eng. 17 (2017) 365-374
[25] Patrick Delobelle, Pascal Robinet, Pol Bouffioux, Philippe Geyer, Isabelle Le Pichon. *A Unified Model to Describe the Anisotropic Viscoplastic Behavior of Zircaloy-4 Cladding Tubes.* Zirconium in the Nuclear Industry: Eleventh International Sypmosium, ASTM STP 1295, E. R. Bradley and G. P. Sabol Eds., American Society for Testing and Materials, 1996, pp. 373-393.
[26] P. V. Shebaldov, M. M. Peregud, A. V. Nikulina, Y. K. Bibilashvilli, A. F. Lositski, N. V. Kuz'menko, V. I. Belov, and A. E. Novoselov, "E1110 Alloy Cladding Tube Properties and Their Interrelation with Alloy Structure-Phase Condition and Impurity Content," Zirconium in the Nuclear Industry: 12thInternational Symposium, ASTM STP 1354, G. P. Sabol and G. D. Moan, Eds., American Society for Testing and Materials, West Conshohocken, PA (2000) 545-559.
[27] Erich Tenckhoff. *Review of Deformation Mechanisms, Texture, and Mechanical Anisotropy in Zirconium and Zirconium Base Alloys.* J. of ASTM Inter., 2, No. 4 (2005). Paper ID JAI12945
[28] Jeong-Whan Yoon, Michael V. Glazoff. *Development of Plasticity Model using Non-Associated Flow Rule for HCP Materials including Zirconium for Nuclear Applications.* INL/EXT-13-29737. (2013)
[29] Y. Yan, T. A. Burtseva, M. C. Billone. *High-Temperature Steam-Oxidation Behavior of Zr-1Nb Cladding Alloy E110.* J. of Nuc. Mat. 393 (2009) 433-448.
[30] Y. Yan, J.R. Keiser, K.A. Terrani, G. L. Bell, L.L. Snead. *Post-Quentch Ductility Evaluation of Zircaloy-4 and Select Iron Alloys under Design Basis and Extended LOCA Conditions.* J. of Nuc. Mat. 448 (2014) 436-440.
[31] Kristina Sadian, Rickard Johansson, Christian Alex. *Consequences of Hydrogen Pick-up in Fuel Cladding: A Literature Study.* Uppsala University (2010).

[32] Y. Yan, T. Smith, Z. Burns, B. Brevard. *Characterization of Local Hydride Re-orientation in High Burn-up PWR Fuel Rods Induced by High Pressure at High Temperaturs.* MRS Fall Meeting presentation. Boston, MA (2016).
[33] J.J.A. DeRuntz, J.P.G. Hodge. *Crushing of a Tube between Rigid Plates.* J. Appl. Mech. 27 (1963) 740-743
[34] R.H. Burton, J.M. Craig. *An Investigation into the Energy Absorbing Properties of etal Tubes loaded in the Transverse Direction.* B.Sc Report, University of Bristol. Bristol, England (1963)
[35] R.G. Redwood. *Crushing of a tube between plates.* J. Appl. Mech. 31 (1964) 357-358.
[36] NRC Draft REGULATORY GUIDE DG-1263. *Establishing Analytical Limits for Zirconium Based Alloy Cladding.* ML 12284A323 (2014)
[37] H. Hooputra, H. Gese, H. Dell, H. Werner. *A Comprehensive Failure Model for Crashworthiness Simulation of Aluminum Extrusions.* Inter. J. of Crashworthiness, 9:5 (2004) 449-464
[38] Spencer D. Snow, Dana K. Morton, Edward L. Pleins, Robert Keating. *Strain-Based Acceptance Criteria for Energy-Limited Events.* 2009 ASME Pressure Vessels and Piping Division Conference (2009) INL/CON-09-15509
[39] Yuanli Bai, Tomasz Wierzbicki. *A New Model of Metal Plasticity and Fracture with Pressure and Lode Dependence.* Inter. J. of Plasticity 24 (2008) 1071-1096
[40] 2017 ASME Boiler & Pressure Vessel Code: Section III Rules for Construction of Nuclear Facility Components. (2017) ASME BPVC.III.A-2017
[41] ABAQUS Documentation, Dassault Systèmes, Providence, RI, USA (2011)
[42] Zirconium Alloys: Properties and Characteristics. *Commissariat à l'Énergie Atomique*, *Grenoble*, *France* (2012).
[43] TREE-NUREG-1180. *Matpro – version 10 A handbook of materials properties for use in the analysis of light water reactor fuel rod behavior* (1978)
[44] Siddharth Suman, Mohd. Kaleem Khan, Manabendra Pathak, R.G. Singh. *Effects of Hydride on Crack Propagation in Zircaloy-4.* 11th Inter. Symposium on Plasticity and Impact Mechanics, Implast. Procedia Engineering 173 (2017) 1185-1190

VITA

Benton Garrison II was born in Nashville, TN to the parents of Benton and Cynthia Garrison. He has one sister: Maleya Garrison. He attended Hendersonville High School in Hendersonville, TN. After graduating, he attended the University of Tennessee Knoxville for his Bachelor of Science in Mechanical Engineering, where he was an undergraduate research assistant for Dr. Eric Wade before graduating with his Bachelor of Science in May 2015. Benton's undergraduate research experience motivated him to further pursue research where he was an intern for his mentor, Dr. Yong Yan, at ORNL, which ultimately motivated him to pursue further education. He accepted his thesis topic on mechanical testing of nuclear materials, and with the guidance of his thesis advisor, Dr. Stephanie TerMaath, completed this research thesis. He graduated with a Master of Science degree in Mechanical Engineering in December 2018. He continues to work at ORNL.